Geochimica et Cosmochimica Acta 344 (2023) 40–58

Contents lists available at ScienceDirect

Geochimica et Cosmochimica Acta

journal homepage: www.elsevier.com/locate/gca

Mass-independent Sn isotope fractionation and radiogenic ^{115}Sn in chondrites and terrestrial rocks

Alessandro Bragagni [a,b,*], Frank Wombacher [a], Maria Kirchenbaur [a,c], Ninja Braukmüller [a,d], Carsten Münker [a]

[a] Institut für Geologie und Mineralogie, Universität zu Köln, Zülpicher Str. 49b, 50674 Köln, Germany
[b] Dipartimento di Scienze della Terra, Università degli studi di Firenze, via La Pira 4, 50121 Firenze, Italy
[c] Institut für Mineralogie, Leibniz Universität Hannover, Callinstraße 3, 30167 Hannover, Germany
[d] Institut für Geologische Wissenschaften, Freie Universität, Malteserstr. 74-100, 12249, Berlin, Germany

ARTICLE INFO

Article history:
Received 9 March 2022
Accepted 14 January 2023
Available online 20 January 2023
Associate editor: Zaicong Wang

Keywords:
Tin isotopes
Mass-independent isotope fractionation
Nucleosynthetic anomalies
Moderately volatile elements
^{115}Sn

ABSTRACT

Tin has ten stable isotopes, providing the opportunity to investigate and discriminate nucleosynthetic isotope anomalies from mass-dependent and mass-independent isotope fractionation. Novel protocols for chemical separation (based on TBP-resin) and MC-ICP-MS analyses are reported here for high precision Sn isotope measurements on terrestrial rocks and chondrites. Relative to the Sn reference standard (NIST SRM 3161a), terrestrial basalts and chondrites show isotope patterns that are consistent with mass-dependent and mass-independent isotope fractionation processes as well as with ^{115}Sn radiogenic ingrowth from ^{115}In.

Two different mass-independent isotope effects are identified, namely the nuclear volume (or nuclear field shift) and the magnetic isotope effect. The magnetic isotope effect dominates in the two measured ordinary chondrites, while repeated analyses of the carbonaceous chondrite Murchison (CM2) display a pattern consistent with a nuclear volume effect. Terrestrial basalts show patterns that are compatible with a mixture of nuclear volume and magnetic isotope effects. The ultimate origin of the isotope fractionation is unclear but a fractionation induced during sample preparation seems unlikely because different groups of chondrites show distinctly different patterns, hence pointing towards natural geo/cosmochemical processes. Only the carbonaceous chondrite Murchison (CM2) shows a Sn isotope pattern similar to what expected for nucleosynthetic variations. However, this pattern is better reproduced by nuclear volume effects. Thus, after considering mass-independent and mass-dependent effects, we find no evidence of residual nucleosynthetic anomalies, in agreement with observations for most other elements with similar half-mass condensation temperatures.

Most chondrites show a deficit in ^{115}Sn/^{120}Sn (typically −150 to −200 ppm) relative to terrestrial samples, with the exception of one ordinary chondrite that displays an excess of about +250 ppm. The ^{115}Sn/^{120}Sn data correlate with In/Sn, being consistent with the β^- decay of ^{115}In over the age of the solar system. This represents the first evidence of the ^{115}In-^{115}Sn decay system in natural samples. The radiogenic ^{115}Sn signature of the BSE derives from a suprachondritic In/Sn$_{BSE}$, which reflects preferential partitioning of Sn into the Earth's core.

1. Introduction

Owing to analytical advances over the last two decades, isotope variations in terrestrial and extra-terrestrial materials were observed for numerous heavy elements. This led to the discovery of mass-dependent and mass-independent isotope fractionation effects, previously unexplored decay systems, and neutron capture effects. Additionally, nucleosynthetic isotope variations were discovered, reflecting variable contributions from different stellar environments. The largest anomalies (up to tens of %) are observed in sub-μm presolar grains (stardust). In bulk meteorites and planetary bodies, nucleosynthetic isotope anomalies are much smaller, typically in the ppm range, and are best observed for refractory elements such as Ca, Cr, Ti, Ni, Zr, Mo, Ba, and Ru (Dauphas et al., 2004, 2014; Andreasen and Sharma, 2006, 2007; Trinquier et al., 2007, 2009; Carlson et al., 2007; Qin et al., 2010; Chen et al., 2010;

* Corresponding author at: Dipartimento di Scienze della Terra, Università degli studi di Firenze, via La Pira 4, 50121 Firenze, Italy.
E-mail address: alessandro.bragagni@unifi.it (A. Bragagni).

https://doi.org/10.1016/j.gca.2023.01.014
0016-7037/

Burkhardt et al., 2011, 2019; Steele et al., 2012; Schiller et al., 2015; Akram et al., 2015; Fischer-Gödde et al., 2015; Elfers et al., 2018; Nielsen et al., 2019). Nucleosynthetic isotope anomalies are usually larger in residues from acid leaching of chondrite powders due to the enrichment of presolar grains in the residues, which are typically enriched in neutron-rich and s-process isotopes (e.g., Rotaru et al., 1992; Dauphas et al., 2002; Hidaka et al., 2003; Schönbächler et al., 2005; Reisberg et al., 2009; Qin et al., 2011; Elfers et al., 2018; Burkhardt et al., 2019). It is currently a matter of debate to which extent nucleosynthetic isotope variations reflect heterogeneities inherited from the molecular cloud (Dauphas et al., 2002) or whether those heterogeneities were generated by thermal processing (e.g., Trinquier et al., 2009) or sorting within the solar system (Regelous et al., 2008; Hutchison et al., 2022).

The half-mass condensation temperature (50% T_C) of Sn was estimated to be 704 K (Lodders, 2003) or 604 K (Wood et al., 2019). As such it is classified as a moderately volatile element (MVE), a group of elements with a 50% T_C between 252 K and 1200 K, i.e. below the 50% T_C of Mg silicates and above that of highly volatile elements (Palme et al., 2014). In contrast to refractory elements, studies on MVE (e.g., Se, Te, Cd, and Hg) generally report no significant nucleosynthetic isotope anomalies between bulk meteorites and Earth (Lauretta et al., 2001; Fehr et al., 2006; Wombacher et al., 2008; Moynier et al., 2009a; Labidi et al., 2018; Toth et al., 2020). Similarly to what is observed on the bulk scale, the MVE isotope composition of leachates resulted in either no isotope anomalies (Toth et al., 2020) or variations that are close to the analytical uncertainty (Fehr et al., 2006; Fukami and Yokoyama, 2017). The lack of nucleosynthetic isotope anomalies in MVE is probably best ascribed to a homogeneous gas phase (Ek et al., 2020). However, the absence of nucleosynthetic isotope anomalies for MVE appears at first glance surprising, given that isotope anomalies for the most volatile elements, the noble gases, and in particular Xe with a 50% Tc = 68 K (Lodders 2003), have been identified early on (Reynolds and Turner, 1964). These anomalies were later related to the s-process (Srinivasan and Anders, 1978) and led eventually to the discovery of presolar grains (Lewis et al., 1987). Three very recent studies (Martins et al., 2022; Savage et al., 2022; Steller et al., 2022) have now revealed nucleosynthetic isotope variations for the moderately volatile element Zn. Nucleosynthetic volatile element isotope variations like those observed for Zn allow to evaluate the sources of volatile elements on Earth and other terrestrial planets (Martins et al., 2022; Savage et al., 2022; Steller et al., 2022). Since hints of nucleosynthetic isotope anomalies have been proposed for Sn (Friebel et al., 2017), further Sn isotope analyses of chondrites and terrestrial samples are needed to evaluate whether nucleosynthetic Sn isotope variations can be well resolved and used to better understand the homogenization of volatile element isotopes after nucleosynthesis and the source of volatile elements to Earth.

With its magic proton number of 50, Sn shows the highest number of stable isotopes (ten) of the whole periodic table and offers the possibility to investigate and discriminate nucleosynthetic isotope anomalies from those introduced by mass-(in)dependent isotope fractionation. Two Sn isotopes are synthesized only by p-process nucleosynthesis (^{112}Sn, ^{114}Sn), ^{124}Sn is only formed by the r-process, while the other seven isotopes (^{115}Sn, ^{116}Sn, ^{117}Sn, ^{118}Sn, ^{119}Sn, ^{120}Sn, ^{122}Sn) have variable contributions from the p-, r- and s-processes. The different proportion of nucleosynthetic processes and the large number of Sn isotopes makes this element a perfect candidate to extend the search for nucleosynthetic isotope anomalies for moderately volatile elements. In their pioneering TIMS work, De Laeter and Jeffery (1965) searched for nucleosynthetic Sn isotope anomalies in iron meteorites. Later, Loss et al. (1990) analyzed acid leachates from the CV3 Allende meteorite and only recently Friebel et al. (2020) published bulk data for the CV3 chondrite Allende using MC-ICP-MS. None of these studies reported significant Sn isotope variations even if evidence of Sn nucleosynthetic isotope variations in bulk and acid leachates of CM and CR chondrites have been presented by Friebel et al. (2017). Nevertheless, there is a clear need for a systematic study on different chondrites with state of the art techniques.

The unequivocal identification of small nucleosynthetic isotopic anomalies can be hampered by stable isotope fractionation. These processes can be natural or induced during sample preparation and consist of mass-dependent isotope fractionation (MDF) and mass-independent isotope fractionation (MIF) (e.g., Wiederhold, 2015 for an overview). Mass-dependent isotope fractionation can induce apparent isotope anomalies if not accurately corrected for by the mass fractionation law used for instrumental mass discrimination correction (e.g., Esat et al., 1986; Wombacher et al., 2004). For example, kinetic isotope separation is described by the kinetic law (which is identical to the exponential law used for instrumental mass discrimination), while equilibrium isotope partitioning follows the equilibrium law (Young et al., 2002). The role of MIF in extraterrestrial material is debated and poorly understood (e.g., Moynier et al., 2013; Dauphas and Schauble, 2016). For the heavy elements, MIF typically fractionates odd from even isotopes, either due to magnetic isotope or nuclear volume effects. MIF in the form of nuclear volume effects are especially pronounced for heavy elements such as Hg, Tl, and U, while the magnetic isotope effect was mainly described for Hg (e.g., Wiederhold, 2015).

The magnetic isotope effect (also called nuclear spin isotope effect) distinguishes between isotopes with or without nuclear spin (Epov, 2011; Epov et al., 2011; Buchachenko, 2018 for reviews). Magnetic isotope effects result from hyperfine coupling between the non-zero nuclear spins of odd nuclei and the magnetic moments of electrons during kinetic reactions (Buchachenko, 2013) and therefore selectively distinguish between isotopes of odd and even mass numbers.

Nuclear volume (or nuclear field shift) effects depend on nuclear volumes (or charge radii) that typically increase with neutron numbers as shown for Sn isotopes in Fig. 1 (Bigeleisen, 1996; Fujii et al., 2006; Schauble, 2007). Since the proton and neutron arrangement is relatively more compact in odd isotopes, a nuclear volume effect is usually best observed when odd and even isotopes are compared. For Sn, however, nuclear volume effects are also predicted for even/even isotopes, especially for neutron-poor and neutron-rich even isotopes (Fig. 1). While nuclear volume effects are expected to be more significant for heavier elements, sub-permil isotope fractionation can still be expected for mid-mass elements like Sn (Schauble, 2013). Nuclear volume effects result from redox changes and are especially pronounced when electrons from the s-orbital are involved (Dauphas and Schauble, 2016), like

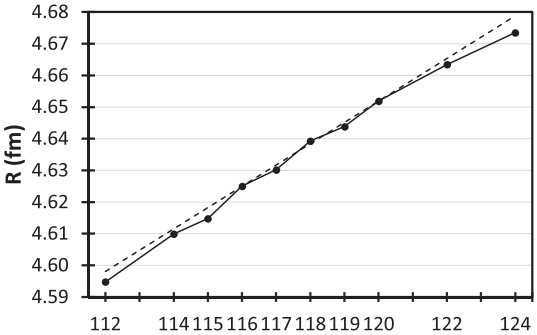

Fig. 1. Nuclear charge radii R in fm (Angeli and Marinova, 2013) vs exact mass of Sn isotopes. A stippled linear line through ^{116}Sn and ^{120}Sn, the two isotopes used for mass discrimination correction, is given for reference.

between Sn^{2+} and Sn^{4+}. Nuclides with larger nuclear radii preferentially partition into phases containing Sn^{4+} (Schauble, 2013). Similarly, during mass-dependent equilibrium isotope partitioning, heavy isotopes partition preferentially into stiffer bonds (Schauble, 2004; Polyakov et al., 2005; Wang et al., 2021a), i.e. those involving Sn^{4+}. Therefore, nuclear volume and mass-dependent equilibrium isotope partitioning act in a similar fashion, resulting in tetravalent Sn being enriched in the higher masses (i.e., heavier and with larger nuclear radii). As a consequence, stable isotope effects ($\delta^{120/116}Sn$) are expected to shift towards the same direction when affected by redox-related equilibrium MDF and nuclear volume effects. With temperature the overall extent of equilibrium MDF and nuclear volume effects decreases, while the contribution of nuclear volume effects relative to equilibrium MDF is expected to increase (Schauble, 2007, 2013).

The pattern of nuclear volume effects can mimic those expected for nucleosynthetic isotope anomalies (Dauphas and Schauble, 2016) and have been proposed as alternative explanations to a nucleosynthetic origin of isotope anomalies in extraterrestrial materials (Fujii et al., 2006; Moynier et al., 2009a, 2013). As such, it is often difficult to unequivocally identify nucleosynthetic anomalies, especially when they are close to the analytical uncertainty (e.g., see the debate about Te nucleosynthetic anomalies in Fehr et al., 2006, 2009; Moynier et al., 2009a). Interestingly, in the case of Sn, the great number of isotopes and the large mass difference (10.7%) allows to distinguish between MIF, MDF, and nucleosynthetic isotope anomalies. Indeed, each process displays a unique Sn isotope pattern, which also permits the discrimination between different MIF processes. After experiments, MIF processes have been proposed to fractionate odd from even isotopes up to 1‰ and 5‰, for nuclear volume (Malinovskiy et al., 2009) and magnetic isotope effects (Moynier et al., 2009b), respectively. With sufficient analytical precision, the two processes can be distinguished on the basis of the even isotopes, which are affected by nuclear volume, but not by magnetic isotope effects.

Another interesting feature of Sn isotopes is the ^{115}In-^{115}Sn decay system. However, the radiogenic ingrowth of ^{115}Sn from ^{115}In (β^- decay; half-life 4.41×10^{14} a, Pfeiffer et al., 1979) has never been observed in natural samples. Even if its applications are limited by its very long half-life, the ^{115}In-^{115}Sn decay system represents a potentially unexplored tool for dating geo-/cosmochemical processes that fractionate In from Sn, for example during early solar system processes. In particular, the In mass fraction of the BSE has been a topic of debate due to its apparent overabundance relative to other similarly volatile elements, resulting in suprachondritic In/Sn_{BSE} (Witt-Eickschen et al., 2009; Wang et al., 2016; Norris and Wood, 2017; Braukmüller et al., 2019). Since the present day $^{115}Sn/^{120}Sn$ of a given reservoir reflects its time integrated In/Sn ratio, the difference in $^{115}Sn/^{120}Sn$ between the BSE and chondrites can provide an independent estimate of the In/Sn_{BSE}.

In this study, we present a new analytical protocol for the chemical separation and purification of Sn and the measurement of its isotope composition. Results on terrestrial materials and chondrites are discussed after modelling possible effects of MDF and MIF processes. Furthermore, we provide the first evidence of the ^{115}In-^{115}Sn decay system in natural samples.

2. Samples, methods and analytical strategies

Four terrestrial samples and 12 chondrite samples were analyzed throughout this study. Terrestrial samples include three intraplate basalts from La Palma (LP1, Kurzweil et al., 2019), Bulgaria (BG 49, Kirchenbaur et al., 2012) and Hawaii (BHVO-2, USGS Reference Materials Program) and one shale (TW50, Wombacher and Rehkämper, 2003). The investigated chondrites are eight carbonaceous chondrites (CV, CO, CM, CK), two ordinary chondrites, one enstatite chondrite, and one Rumuruti chondrite. The analysed chondrites are falls (CV3 Allende, CO 3.8 Isna, CO Kainsaz, CM2 Murchison, and LL3.4 Chainpur), desert finds (CV3 NWA 3118, CV3 Acfer 082, CO3 Dar al Gani 067, R3.9 NWA 753, H3.4 Roosevelt) and Antarctic finds (CK ALH 85002 and EL3 MAC 88136). After removing fusion crust and weathered surfaces, chondrite samples were milled with a Fritsch Pulverisette 23. For carbonaceous chondrites, it has been shown that weathering does not significantly affect Sn (Braukmüller et al., 2018). However, since we cannot exclude a priori an effect of weathering, samples were selected to minimize such a risk. For instance, both Antactic finds are weathering grade A, and, according to the Meteoritical Bulletin, CV3 NWA 3118 has "low weathering grade" and R3.9 NWA 753 has weathering grade W2 "making it one of the freshest Rumuruti chondrites". Indium and Sn mass fractions of chondrites were determined using two different methods. Some of the In and Sn mass fractions were determined by isotope dilution ICP-MS (Braukmüller et al., 2020), while the remaining data were obtained with conventional ICP-MS measurements at the Universität zu Köln using an iCAP Q ICP-MS in combination with a PFA nebulizer and spray chamber. Conventional ICP-MS measurements were performed by external calibration to multi-element chondrite calibration solutions (Braukmüller et al., 2018) using Rh as an internal standard.

2.1. Testing Sn loss in different acid media

Procedures for sample digestion and purification of Sn have to take into account possible Sn loss due to volatilization and precipitation of insoluble Sn phases due to oxidation. Moreover, in order to ensure a consistent chemical behavior, it is important that Sn is only present in the 4+ oxidation state, avoiding the formation of reduced Sn^{2+} species. At strongly oxidizing conditions, Sn forms SnO_2 (cassiterite), which is extremely difficult to (re)-dissolve (Yamazaki et al., 2013). Volatile loss of Sn into the gas phase can also occur during dry down steps (boiling point of $SnCl_4$ = 114 °C) . To test which conditions in the laboratory can diminish the recovery of Sn, we performed evaporation tests in different acid media (HCl, HNO_3, HCl + HNO_3, $HClO_4$), temperatures (90, 110, 140, 180 °C), and matrices (i.e., without matrix, artificial matrix with selected elements, basaltic matrix). Our tests, described and discussed in the Supplementary material, indicate that drying down HNO_3 solutions with only Sn can result in Sn loss. In contrast, solutions containing an artificial matrix or a basaltic matrix along with Sn, did not result in Sn loss. For this reason, HF was always added before evaporating the Sn solutions eluted in HNO_3 from the exchange resins.

2.2. Sample digestion

Acids used (HCl, HF, HNO_3) were purified in PFA distills and HCl was further purified using anion exchange chromatography (Kirchenbaur et al., 2018; Braukmüller et al., 2020). Up to 200 mg of sample powder were dissolved in 15 ml PTFE beakers, using up to 8 ml of an 1:1 mixture of HNO_3 (14 M) and HF (24 M). In the case of meteorite samples, this digestion step was performed in Parr pressure digestion vessels, which were placed inside an oven at 180 °C for at least 2 days. Since basalts are generally devoid of phases that require high pressure digestion, samples LP1, BG49, and BHVO-2 were dissolved in closed 15 ml PFA beakers placed on a hotplate at 120 °C for at least two days. After the HF-HNO_3 digestion, sample solutions were dried down (80–100 °C) and treated three times with 14 M HNO_3 to remove residual fluorides: twice adding 1 ml 14 M HNO_3 and evaporating

directly, and once adding about 5 ml 14 M HNO_3 and leaving the beakers closed overnight on the hotplate at >100 °C or, in the case of meteorites, in Parr pressure vessels at 180 °C in an oven. After evaporating the HNO_3 (80–100 °C), sample solutions were dried down two more times with 14 M HNO_3 before converting the sample cations into the chloride form using 6 ml 6 M HCl. At this stage the sample solution was clear with no visible solid residue. Samples were then dried down once more and re-dissolved for ion exchange chromatography. Additional digestions of terrestrial samples were performed with larger amounts of powders (up to 2.5 g) following a similar procedure but using 60 ml PTFE vials and increasing the volume of reagents. importantly, to minimize Sn loss, every evaporation step was performed at <110 °C and beakers were removed from the hotplate shortly after reaching dryness.

2.3. Chemical separation

The chemical separation was performed in two steps. The first step employs an anion exchange column chromatography modified after Wang et al. (2017). The samples were loaded in 0.4 M HCl onto 2 ml Bio-Rad polypropylene columns filled with 2 ml of Bio-Rad AG1-X8 (200–400 mesh) anion exchange resin. Matrix elements were then eluted with 0.4 M HCl, before collecting Sn in 0.5 M HNO_3. The volume of acid used for loading (1–4 ml) and eluting the matrix (30–40 ml) varied depending on the sample size. Some samples were loaded in 1 M HCl, instead of 0.4 M HCl, similar to the procedure of Friebel et al. (2020) and collected in 1 M HNO_3 (Asai et al., 2013). These modifications were done after some samples yielded a poor Sn recovery (50–70%). However, the changes did not show a significant improvement as they sometimes also resulted in erratic low yields. The typical procedure for 200 mg samples is described in Table 1, and an elution curve obtained from a basalt sample passed through the anion exchange resin is reported in Supplementary Fig. S2A. After collecting the Sn cut, 0.1 ml of 24 M HF was immediately added into the beaker to avoid possible Sn precipitation (Yamazaki et al., 2013). The solution was subsequently dried down and treated twice with 0.1 ml of a H_2O_2-HNO_3-HF mixture (5:10:1) to attack organics eluted from the resin.

The second step of the chemical separation makes use of the TBP resin that has been recently developed by Triskem. It is based on tributyl phosphate (TBP), which shows a strong affinity for Sn (Akaza and Yata, 1983). To our knowledge, this represents the first application in geo-/cosmochemistry of this particular resin. The TBP resin protocol used in this study is based on Dirks et al. (2014) and the elution curve obtained from a multielement solution is reported in Supplementary Fig. S2B. Additional tests performed on TBP resin are reported in the Supplementary material along with a comparison between TBP and TRU-spec, which is commonly used for Sn separation (e.g., Yamazaki et al., 2013; Creech et al., 2017; Kirchenbaur et al., 2018; Friebel et al., 2020). Custom made columns (from 1 ml PE Pasteur pipettes) were filled with 0.8 ml TBP resin on top of 0.2 ml Triskem pre-filter material. Samples were loaded in 2 ml 2 M HCl. Most matrix elements were not retained on the resin and were washed out in 2 M HCl, while Sn was eluted subsequently in 0.1 M HCl. In some tests, Sn eluted earlier than expected, similar to what was observed by Andris and Beňa (2016). In order to minimize any Sn loss, the intermediate step in 1 M HCl proposed by Dirks et al. (2014) was skipped and the 2 M HCl matrix elution was reduced to only 10 ml. The most critical interfering elements Cd, In, and Te were efficiently removed during the TBP resin step, but traces of these elements were sometimes detected by quadrupole ICP-MS in the final Sn cut. The occurrence of these elements was possibly due to the limited amount of 2 M HCl used before collecting Sn. To overcome this issue, in some cases, the TBP resin procedure was repeated a second time. The final Sn cut was then dried down and treated twice with 0.1 ml of H_2O_2-HNO_3-HF mixture (5:10:1) and re-dissolved in a 0.56 M HNO_3-0.24 M HF solution for mass spectrometry.

Three full procedural blanks yielded 0.4 to 0.6 ng of Sn. Since each sample contains at least 100 ng of Sn, any blank contribution was negligible. Full procedural yields of samples larger than 200 mg were relatively low (especially for LP1), with an average of 67%, while typical samples of maximum ca. 200 mg resulted in higher yields, with an average of about 80%.

2.4. Mass spectrometry

Samples were measured with a Thermo Scientific Neptune Plus MC-ICP-MS at the Universität zu Köln. Sample solutions were introduced using a Cetac Aridus II membrane desolvating system in combination with a Cetac C-Flow (100 µl/min flow rate) or an ESI MicroFlow PFA-100 nebulizer. For all measurements, standard Ni sample and H skimmer cones were used. Standard and sample

Table 1
Column chemistry separation used for the purification of Sn.

2 ml AG1-X8 in 2 ml BioRad column			*0.8 ml of TBP resin and 0.2 ml Eichrom Pre-filter material in 1 ml PE Pasteur pipette*		
	reagent	volume (ml)		reagent	volume (ml)
Cleaning	8 M HCl	10	*Cleaning*	0.1 M HCl	7
	H_2O	10		2 M HCl	7
	0.5 M HNO3	10		0.1 M HCl	7
	H_2O	10			
	0.4 M HCl	10			
Conditioning	0.4 M HCl	6	*Conditioning*	2 M HCl	2 × 2
Sample loading	0.4 M HCl	4	*Sample loading*	2 M HCl	2
	0.4 M HCl	5 + 5 + 10		2 M HCl	4
	0.4 M HCl	5 + 5		2 M HCl	3 × 2
Collecting	0.5 M HNO3	3 × 4.7	*Collecting*	0.1 M HCl	4 × 1
Cleaning	0.5 M HF	10	*Cleaning*	0.5 M HNO3	7
	H_2O	10		H_2O	7
	0.5 M HNO3	10		0.1 M HCl	7
	H_2O	10			
	8 M HCl	10			
	0.5 M HCl	10			
	H_2O	10			

The reported procedure is optimized for 200 mg samples. If larger samples were processed, the volume loaded onto the first column was increased. The second step was sometimes repeated twice in order to improve the separation of Sn from interfering elements.

solutions were analyzed at 75 or 50 ng/ml, with signal intensities on ^{120}Sn between 8 and 17 V. The number of collectors on the MC-ICP-MS instrument is limited to nine. In order to collect signals for every Sn isotope and the additional masses for interference correction, samples were analyzed in separate analytical sessions using two different collector configurations (Fig. 2). One configuration (L) was used to collect the signals from the lower mass isotopes of Sn (112, 114, 115, 116, 118, 119, 120) and that of m/z 111 and 113 to monitor Cd and In isobaric interferences, respectively. In the second configuration (H), the six heavier isotopes of Sn (117, 118, 119, 120, 122, 124) were measured along with ^{125}Te and ^{126}Te to monitor interferences from Te isobars. In both configurations, Sn isotopes were measured using amplifiers with 10^{11} Ω resistors, with the exception of ^{120}Sn, where a 10^{10} Ω resistor was used in the first analytical sessions. For Cd, In, and Te interference monitors, 10^{13} Ω resistors were applied. Each measurement consists of 60 cycles with 4 s integration times each. The ion current signals were corrected for the amplifier gain and electronic baselines (1200 s), which were taken before each measurement session, whereby the baseline was determined about one hour after the gain calibration to make sure that no residual gain signal was collected with 10^{13} Ω resistors in place. The instrumental mass discrimination was corrected using the exponential law and internal normalization to ^{116}Sn/^{120}Sn = 0.4460 (Devillers et al., 1983). The Sn isotope ratios are reported in the μ-notation, representing the average parts-*per*-million deviations relative to the NIST SRM 3161a standard solution, which was measured before and after each sample (standard-sample bracketing technique):

$$\mu^{1xx/120}Sn_{SRM3161a} = 10^6 \times \left(\frac{R_{1xx/120}}{R^{SRM3161a}_{1xx/120}} - 1\right) \quad (1)$$

whereby 1XX indicates Sn isotopes in the numerator. For simplicity and due to the consistent denominator (^{120}Sn) and reference standard (NIST SRM 3161a), the expression $\mu^{1xx/120}Sn_{SRM\ 3161a}$ is later replaced by μ^{1xx}Sn. In addition, the δ-notation is adopted to estimate stable isotope fractionation. It refers to the offset in the ^{120}Sn/^{116}Sn of the samples relative to the average of the bracketing NIST SRM 3161a values and it is expressed as:

$$\delta^{120/116}Sn_{SRM3161a} = 10^3 \times \left(\frac{R_{120/116}}{R^{SRM3161a}_{120/116}} - 1\right) \quad (2)$$

Samples were accurately diluted to match the signal of the samples to that of the bracketing NIST SRM 3161a standard solution to within 10%. After each analysis, a rinse solution (0.56 M HNO_3-0.24 M HF) was aspired for four minutes. On-peak baselines were taken before each analysis to monitor the background evolution. The Sn background increased during each analytical session but it never exceeded a signal intensity of 15 mV on ^{120}Sn. The background signals show relative intensities that resembles the isotopic composition of Sn, therefore excluding significant contribution from polyatomic interferences formed in the plasma such as $^{40}Ar_3^+$ (m/z = 120). Since measurements were performed with a ^{120}Sn signal between 8 and 17 V, any contribution of the background signal is negligible and no correction was applied. As $^{238}U^{2+}$ can interference on ^{119}Sn, U was monitored, resulting in U^{2+}/U = 0.4%. The generation of Sn oxides (i.e. SnO/Sn) was <0.1%.

2.5. Interference correction

The 120, 122, and 124 m/z signals require a Te interference correction. Two Te isotopes were monitored during the analyses: ^{126}Te is more abundant (18.8%) than ^{125}Te (7.07%) but m/z 126 coincides with a minor isotope of Xe (0.09%), which could be present as an impurity in the Ar supply. Mass scans performed in "rinse" solutions show no signal on m/z 126 but a peak on m/z 125. This testifies the lack of a significant Xe interference on m/z 126 but also the occurrence of an unknown interference on m/z 125, which was also observed by Wang et al. (2017) and Friebel et al. (2020). Friebel et al. (2020) concluded that the source was $^{124}SnH^+$, but in our cases a hydride origin can be excluded as the corresponding ion beam signals were not observed on m/z 121 ($^{120}SnH^+$) or 123 ($^{122}SnH^+$). Wang et al. (2017) did not speculate on the origin of such an interference but stated that it was "an unknown constantly formed molecule". Our observations suggested that the extent of the interference is influenced by the N_2 gas flow of the Aridus II. In particular, the interference appears above a certain value of N_2. Therefore, during each analytical session, the N_2 gas flow was tuned to minimize the interference on ^{125}Te and potentially additional interferences that could directly affect Sn isotope signals. In fact, it is not possible to exclude the presence of similar interferences on Sn isotope masses due to the inability of fully washing out the Sn signal. The Te contribution on m/z 120, 122, 124 is estimated from ^{125}Te or ^{126}Te and using the ^{118}Sn/^{120}Sn ratio (not corrected for ^{120}Te) to mimic the instrumental mass discrimination on Te isotope ratios. The difference between the corrections performed with ^{125}Te or ^{126}Te are mostly within the analytical uncertainty. The reliability of the Te interference correction was checked using a Sn solution doped with Te. The results of these tests, which were performed in four different analytical sessions, are reported in Supplementary Fig. S3. At least

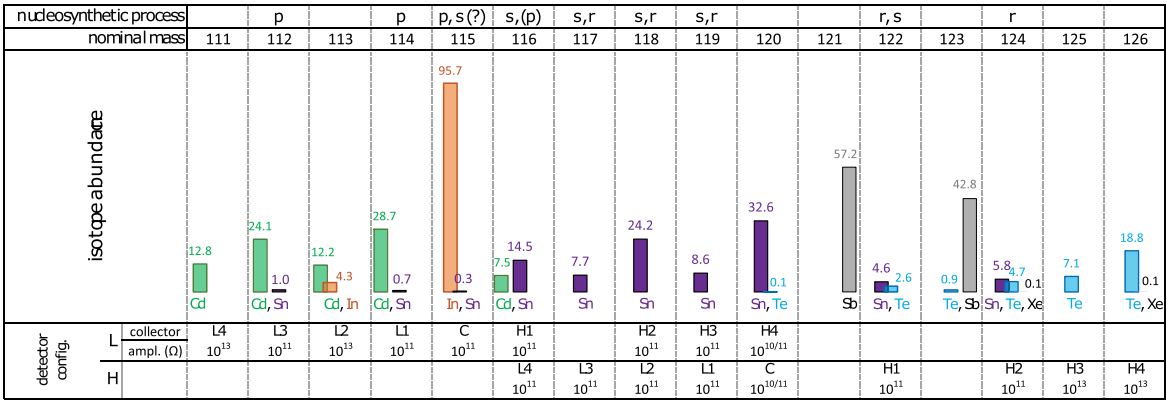

Fig. 2. Relative abundances (%) of isotopes in the mass range of Sn and measured masses. Two distinct collector configurations are used, one for light masses (L), and one for heavy masses (H). The figure illustrates the axial positions of each measured mass and the type of resistor used at the amplifiers. The top line reports the nucleosynthetic processes for Sn isotopes.

up to $^{126}Te/^{120}Sn$ = 0.002 there is no evidence for inaccurate Te interference corrections on $^{122}Sn/^{120}Sn$ and $^{124}Sn/^{120}Sn$. As seen from Supplementary Fig. S3, Te corrections performed with ^{125}Te are mostly indistinguishable from that obtained with ^{126}Te. In order to avoid any possible issue due to the unknown interference on mass 125, data are reported using the correction based on ^{126}Te. As mentioned earlier, mass scans of "rinse solutions" did not reveal a signal on *m*/*z* 126, attesting the lack of significant signals of the two similar abundant ^{126}Xe and ^{124}Xe isotopes. Significant effects of ^{124}Xe interferences are also excluded by the similar $^{124}Sn/^{120}Sn$ measured in 50 and 75 ppb bracketing NIST SRM 3161 solutions during the same analytical session. This is because the ^{124}Xe interference, which is constant, would have a larger effect on the smaller Sn signal. Moreover, since the signals of the bracketing NIST SRM 3161 and that of the samples was always matched between 10%, at least 90% of any residual ^{124}Xe contribution is cancelled by the sample/standard technique. For the above reasons, we considered Xe interferences negligible.

The signals for ^{112}Sn, ^{114}Sn, and ^{116}Sn, suffer from Cd isobaric interferences. Cadmium contribution on these ion beams are calculated using the ^{111}Cd signal and assuming a mass bias based on the measured $^{118}Sn/^{120}Sn$ ratio. NIST SRM 3161a solutions doped with variable amounts of Cd show that this correction is reliable up to $^{111}Cd/^{120}Sn$ = 0.0002 (Supplementary Fig. S3). The least abundant isotope of Sn, ^{115}Sn (0.34%), is affected by the isobaric interference of ^{115}In (abundance of 96%). In addition, ^{113}In, which is used to monitor the In signal, is in turn affected by the interference from ^{113}Cd. Therefore, a quantitative In interference correction on the ^{115}Sn signal is challenging. As observed by Friebel et al. (2020), the uncertainty on the $^{115}Sn/^{120}Sn$ ratio is strongly influenced by the In interference correction. The main reason resides in the much larger abundance of ^{115}In relative to ^{113}In ($^{115}In/^{113}In$ = ca. 22). Thus, any uncertainty associated with the ^{113}In signal is amplified ca. 22 times. The ^{113}In correction was tested with Sn NIST SRM 3161a standard solutions doped with variable concentrations of Cd and In, including also solutions with both In and Cd. As observed in Supplementary Fig. S3, solutions doped with Cd do not show variations from the reference $^{115}Sn/^{120}Sn$ up to $^{111}Cd/^{120}Sn$ = 0.0001. A similar limit for In doped solutions can be set at $^{113}In/^{120}Sn$ = 0.00001. Solutions doped with both In and Cd provide the opportunity to test the In correction in more realistic conditions, i.e. in samples containing different proportions of both elements. The two solutions having $^{111}Cd/^{120}Sn$ and $^{113}In/^{120}Sn$ below the limits defined by Cd-Sn and In-Sn solutions do not deviate from the reference values (Supplementary Fig. S3). The other four solutions that have higher $^{111}Cd/^{120}Sn$ and $^{113}In/^{120}Sn$ show deviations that are similar or lower than those observed in solutions doped with only Cd or In. Therefore, the limits on $^{111}Cd/^{120}Sn$ and $^{113}In/^{120}Sn$ defined by In-Sn and Cd-Sn solutions are expected to be applicable to conditions where both Cd and In are present, but below we will report additional problems related to Cd and In interference corrections on ^{115}Sn for real samples.

3. Results

During each analytical session, after mass discrimination correction the bracketing NIST SRM 3161a solution shows variations (2RSD) of 39–87 ppm for $^{112}Sn/^{120}Sn$, 33–75 ppm for $^{114}Sn/^{120}Sn$, 61–119 ppm for $^{115}Sn/^{120}Sn$, 9–17 ppm for $^{117}Sn/^{120}Sn$, 6–14 ppm for $^{118}Sn/^{120}Sn$, 8–27 ppm for $^{119}Sn/^{120}Sn$, 15–36 ppm for $^{122}Sn/^{120}Sn$, and 18–89 ppm for $^{124}Sn/^{120}Sn$. With the exception of $\mu^{115}Sn$, single sample measurements of $\mu^{1xx}Sn$ show < 90 ppm variation from the bracketing NIST SRM 3161a solution. Replicate analyses of LP1 can be used to estimate the intermediate precision (often referred as external reproducibility) of the method. Multiple digestions and measurements of LP1 yielded a 2SD of 54 ppm for $\mu^{112}Sn$, 68 ppm for $\mu^{114}Sn$, 101 ppm for $\mu^{115}Sn$ (uncorrected for In interference, while on the corrected $\mu^{115}Sn$ the 2SD is 516 ppm), 16 ppm for $\mu^{117}Sn$, 11 ppm for $\mu^{118}Sn$, 15 ppm for $\mu^{119}Sn$, 20 ppm for $\mu^{122}Sn$, and 29 ppm for $\mu^{124}Sn$ (Table 2). These 2SD are used to estimate the uncertainty for single measurements, i.e. for samples that were measured only once. The averages of samples that were analysed multiple times are better constrained and their uncertainty is estimated dividing the 2SD intermediate precision obtained from LP1 by the square root of *n*, where *n* is number of available measurements. In addition, when at least four sample measurements are available, we also estimate the Student-t 95% confidence interval (Table 2 and Table 3, Fig. 3 and Fig. 4). In the figures and in the text we use both uncertainty estimates and we consider significant only variations that are larger than both estimates (Fig. 3 and Fig. 4).

The isotope composition of NIST SRM 3161a processed through chemical separation (total Sn = 400 ng) and doped procedural blanks (100 ng of NIST SRM 3161a added after the chemical separation) are indistinguishable from the unprocessed NIST SRM 3161a solution (Supplementary Table S1, Supplementary Fig. S4).

The three terrestrial basalts (LP1, BG49, BHVO-2) show similar average isotope patterns. For example, LP1 has negative $\mu^{117}Sn$ (−13 ± 3), $\mu^{119}Sn$ (−15 ± 2), $\mu^{122}Sn$ (−7 ± 3), and $\mu^{124}Sn$ (−14 ± 5) relative to NIST SRM 3161a (Table 2, Fig. 3). The shale TW50 shows average values that deviate by <5 $\mu^{1xx}Sn$ and overlap with NIST SRM 3161a within analytical uncertainty.

A more complex picture emerges from the average isotope patterns of different chondrites (Table 3, Fig. 4). Regarding $\mu^{117}Sn$ and $\mu^{119}Sn$, negative shifts are observed for OC and CM chondrites (∼-20), while CV and CO resulted in smaller deviations from the bracketing solution that cannot be considered significant with the exception of $\mu^{117}Sn$ in CV chondrites, which yielded +31 ± 27. However, this is due to three samples (two digestions of Allende and one of NWA 3118) that yielded unusually high $\mu^{117}Sn$, between +75 and + 85. Without these three samples, the average $\mu^{117}Sn$ of CV chondrites decreases to +6 ± 8, which is similar to that of $\mu^{119}Sn$ (+5 ± 4) and it overlaps with the composition of NIST SRM 3161a. Unlike terrestrial basalts, chondrites with negative $\mu^{117}Sn$ and $\mu^{119}Sn$ do not always show similar offsets in $\mu^{122}Sn$ and $\mu^{124}Sn$. In fact, OC show the most negative anomaly in $\mu^{117}Sn$ and $\mu^{119}Sn$ but no clear anomaly in $\mu^{122}Sn$ and $\mu^{124}Sn$ (although one measurement of Roosevelt yielded negative $\mu^{122}Sn$ and $\mu^{124}Sn$). In contrast, Murchison (CM2), which also has negative $\mu^{117}Sn$ and $\mu^{119}Sn$, yielded the most negative average $\mu^{122}Sn$ and $\mu^{124}Sn$. No clear offset from NIST SRM 3161a is observed in $\mu^{122}Sn$ and $\mu^{124}Sn$ for CV and CO chondrites. Only one sample was processed for Rumuruti-type, Enstatite and CK chondrites, respectively. The latter two do not show clear anomalies. The Rumuruti-type chondrite, however, displays some of the largest variations recorded in our dataset, with a U-shaped isotope pattern, characterized by the highest measured $\mu^{112}Sn$, $\mu^{122}Sn$ and $\mu^{124}Sn$ and slightly negative $\mu^{117}Sn$ and $\mu^{119}Sn$.

The ^{115}Sn data requires additional considerations concerning the interference correction. In Fig. 5A, the In-corrected (open symbols) and In-uncorrected (filled symbols) $\mu^{115}Sn$ values for terrestrial rocks and NIST SRM 3161a are plotted against the ^{113}Cd corrected $^{113}In/^{120}Sn$ signal. In terrestrial samples, the In-corrected $\mu^{115}Sn$ show larger scatter and some bias towards higher values in comparison to the uncorrected ones (Fig. 5B–C). For LP1, the estimated intermediate precision (or external reproducibility) is 516 ppm on In-corrected $\mu^{115}Sn$ and 101 ppm for the In-uncorrected $\mu^{115}Sn$. Friebel et al. (2020) also reported high uncertainty for In corrected ^{115}Sn measurements and decided to use In-uncorrected data. The reliability of In-uncorrected data was

Table 2
Tin isotope data of terrestrial rocks.

	$\mu^{112}Sn$	$\mu^{114}Sn$	$\mu^{115}Sn$ *^{115}In uncorr.*	$\mu^{115}Sn$ *^{115}In corr.*	$\mu^{117}Sn$	$\mu^{118}Sn$ *L config.*	$\mu^{118}Sn$ *H config.*	$\mu^{118}Sn$ *L + H config*	$\mu^{119}Sn$ *L config.*	$\mu^{119}Sn$ *H config.*	$\mu^{119}Sn$ *L + H config*	$\mu^{122}Sn$	$\mu^{124}Sn$	$\delta^{120}Sn/^{116}Sn$ *L config.*	$\delta^{120}Sn/^{116}Sn$ *H config.*	$\delta^{120}Sn/^{116}Sn$ *L + H config*
LP1																
avg ± 2 s.e.	−2 ± 11	−3 ± 14	8 ± 25	161 ± 129	−13 ± 3	2 ± 2	0 ± 2	1 ± 1	−15 ± 3	−15 ± 3	15 ± 2	−7 ± 3	0 ± 5	0.2 ± 0.1	0.1 ± 0.1	0.2 ± 0.1
2SD	54	68	101	516	16	9	12	11	13	17	15	20	29	0.6	0.1	0.1
n	25	25	16	16	36	25	36	61	25	36	61	36	36	25	36	61
BG49																
avg	−4 ± 12	−17 ± 17	−27 ± 19	63 ± 64	−15 ± 5	0 ± 2	3 ± 2	1 ± 2	−13 ± 4	−14 ± 3	−13 ± 1	−9 ± 8	−17 ± 6	0.1 ± 0.2	0.2 ± 0.1	0.2 ± 0.1
n	16	16	16	9	13	16	13	29	16	13	29	13	13	16	13	29
BHVO-2																
avg	−25	−15	−11	62	−6	1	7	4 ± 7	−18	−7	−13 ± 4	−7	−28	0.5	0.3	0.4 ± 0.1
n	3	3	3	1	3	3	3	6	3	3	6	3	3	3	3	6
TW50																
avg	1 ± 17	−5 ± 28	−57 ± 58	152 ± 214	−3 ± 11	6 ± 4	−2 ± 5	2 ± 4	0 ± 7	−5 ± 9	−3 ± 2	−2 ± 11	−3 ± 13	0.2 ± 0.2	0.2 ± 0.2	0.2 ± 0.1
n	5	5	5	5	5	5	5	10	5	5	10	5	5	5	5	10

Uncertainties are reported as 2 SD and 2 s.e. for LP1, the sample used to assess the intermediate precision (or external reproducibility). For other samples, the uncertainties are reported only when at least four measurements are available and are expressed as two-sided Student's-t 95% confidence intervals. $\delta^{116}Sn/^{120}Sn$ expresses the per mill variations relative to the bracketing SRM3161a. $\delta^{116}Sn/^{120}Sn$ expresses the per mill variations relative to the bracketing NIST SRM3161a. Individual measurements are reported in Table S1.

assessed by the similar results obtained on chemically processed Sn reference solutions and rock samples. Likewise, in our case the two measurements of chemically processed NIST SRM 3161a yielded In-uncorrected $\mu^{115}Sn$ undistinguishable from the bracketing NIST SRM 3161a and the four terrestrial rocks (Fig. 5, Supplementary Table S1). In other words, In-uncorrected data do not seem to be affected by ^{115}In interferences because different terrestrial samples and chemically processed NIST SRM 3161a show consistent results, which are similar to that of the bracketing solution. In order to further evaluate the possible occurrence of ^{115}In interference we consider the measured $^{113}In/^{120}Sn$. Due to the isobaric interference of ^{115}In on ^{115}Sn, a correlation between $^{113}In/^{120}Sn$ and $\mu^{115}Sn$ is expected for the In-uncorrected values. However, regardless of $^{113}In/^{120}Sn$, In-uncorrected $\mu^{115}Sn$ values scatter around zero and do not plot along the expected trend (dotted line in Fig. 5A). This affirms that, at the scale of the precision of the method, the majority of the samples show a negligible contribution of ^{115}In on m/z 115, regardless of $^{113}In/^{120}Sn$. The lack of evidence for ^{115}In interference, confirms that the In correction is not needed and that In-uncorrected data are reliable. However, this implies also that the $^{113}In/^{120}Sn$ might be sometimes overestimated. The reasons are not clear but, since the 113 m/z signal is dominated by ^{113}Cd (Supplementary Table S1) and ^{113}In seems to be minor, the Cd interference correction on the 113 m/z signal might not be accurate enough, even though Cd/Sn is always below the threshold of $^{111}Cd/^{120}Sn$ = 0.0001 defined above. Possible reasons include (i) the wrong determination (or drift) of the amplifier gains or baselines on m/z 111 and/or 113, (ii) the presence of Cd (or In) with an isotope composition different to what is assumed, (iii) an unknown interference on m/z 113. Regarding In-corrected $\mu^{115}Sn$ data, it can also be noted that they trend towards positive values (Fig. 5A–C). This is likely related to the problems in correctly estimating $^{113}In/^{120}Sn$ but a proper evaluation is further complicated by the fact that the ^{115}In correction, when used, was also applied to the bracketing solution. Regardless, In-uncorrected $\mu^{115}Sn$ data seem to be robust, not being significantly affected by ^{115}In signals as attested by the lack of correlation with $^{113}In/^{120}Sn$ (^{113}Cd corrected) (Fig. 5A). Therefore, hereafter only ^{115}In uncorrected data are discussed.

Pooled measurements of terrestrial samples yielded $\mu^{115}Sn$ values indistinguishable (LP1: 8 ± 25 2 s.e.; TW50: 50 ± 58) or slightly lower (BG49: −27 ± 19) than the bracketing NIST SRM 3161a (Fig. 5D and Table 2). Chondrites clearly point towards lower $\mu^{115}Sn$. Most of the carbonaceous chondrites show negative $\mu^{115}Sn$, resulting on an average $\mu^{115}Sn$ −158 ± 38 (2 s.e.). The LL3.4 ordinary chondrite Chainpur resulted in the highest $\mu^{115}Sn$ (+279 ± 101), while the two measurements of the H3.4 Roosevelt yielded a negative $\mu^{115}Sn$ similar to that of carbonaceous chondrites and the only measured Rumuruti and enstatite chondrites (Fig. 5D).

In Table 2 and Table 3 we also report mass-dependent $^{120}Sn/^{116}Sn$ variations (i.e. uncorrected for mass bias) measured between samples and the bracketing NIST SRM 3161a solution as $\delta^{120/116}Sn$. Overall, $\delta^{120/116}Sn$ sample data scatter around zero with an uncertainty for single measurements of ± 0.6 as estimated from the 2SD of replicate measurements of LP1. A notable exception is represented by the Rumuruti chondrite NWA 753, which yielded $\delta^{120/116}Sn$ = −2.0 ± 0.6 in both measurements (H and L mass configurations).

Regarding In and Sn mass fractions, the differences between isotope dilution and conventional ICP-MS data are smaller than 10% (Supplementary Table S2). Similar variations are also observed within replicate digestions, most likely mainly reflecting heterogeneity of the sample powders. Overall, Sn shows a limited range in mass fractions in the analyzed chondrites, varying between 0.44 and 1.04 μg/g. A larger spread is observed for In mass fractions

Table 3
Tin isotope data of chondrites.

	type	sample weight (mg)	μ ^{112}Sn	μ ^{114}Sn	μ ^{115}Sn ^{115}*In* uncorr.	μ ^{115}Sn ^{115}*In* corr.	μ ^{117}Sn	μ ^{118}Sn *L config.*	μ ^{118}Sn *H config.*	μ ^{118}Sn *avg*	μ ^{119}Sn *L config.*	μ ^{119}Sn *H config.*	μ ^{119}Sn *avg*	μ ^{122}Sn	μ ^{124}Sn	δ^{120}Sn/^{116}Sn *L config.*	δ^{120}Sn/^{116}Sn *H config.*	δ^{120}Sn/^{116}Sn *avg*	
uncertainty single measurement			*± 54*	*± 68*	*± 101*	*± 516*	*± 16*	*± 9*	*± 12*		*± 13*	*± 17*		*± 20*	*± 29*	*± 0.6*	*± 0.6*		
Allende	CV3	396	27	31	−133	−168	4	6	1	3	4	0	2	0	−8	−0.2	0.1	0.0	
Allende *(r)*	CV3	396	−16	34	−152	−62		9		9	5		5			−0.1		−0.1	
Allende	CV3	201	−26	32	−36	292	14	17	6	11	10	14	12	19	3	0.0	−0.1	0.0	
Allende	CV3	201					−2		−1	−1		0	0	7	1		0.3	0.3	
Allende	CV3	201	33	10			1	13	−2	5	16	9	12	7	3	0.7	0.5	0.6	*
Allende	CV3	200	18	4	−106		85	13	6	10	3	1	2	4	−9	0.0	−0.1	0.0	**
Allende	CV3	200	8	−58	−149		79	−7	2	−3	−10	−7	−9	13	4	0.0	0.0	0.0	**
Allende	CV3	200	−4	−16	−165	−152	19	1	7	4	10	0	5	−6	−25	0.1	0.2	0.1	
NWA 3118	CV3	399	3	−17	−171	−131	75	1	−1	0	4	−1	1	34	19	−0.6	−0.8	−0.7	
Acfer 082	CV3	346	−15	18	12	354	3	2	4	3	1	−10	−5	0	11	−0.6	−0.6	−0.6	
CV avg			**3 ± 15**	**4 ± 22**	**−112 ± 52**	**22 ± 227**	**31 ± 27**	**6 ± 5**	**2 ± 3**	**4 ± 3**	**5 ± 5**	**1 ± 5**	**3 ± 1**	**9 ± 9**	**0 ± 9**	**−0.1 ± 0.3**	**0.0 ± 0.3**	**−0.1 ± 0.2**	
CV selected avg			**0 ± 24**	**18 ± 19**	**−95 ± 87**	**53 ± 279**	**6 ± 8**	**8 ± 6**	**2 ± 4**	**5 ± 3**	**8 ± 5**	**2 ± 8**	**5 ± 2**	**4 ± 8**	**−2 ± 12**	**0.0 ± 0.4**	**0.1 ± 0.4**	**0.0 ± 0.2**	
ALH85002	CK	350	6	7	−256	132	−9	−5	−13	−9	5	1	3	9	13	−0.3	−0.6	−0.5	
Isna	CO3.8	408	−5	−14	−186	173	−4	4	5	5	−2	5	1	−1	−1	0.2	0.0	0.1	
Dar al Gani 067	CO3	404	−12	−34	−259	55	−5	11	4	7	−10	−10	−10	−3	5	0.0	−0.3	−0.1	
Kainzas	CO	196	45	91	−79	−883	−2	0	5	2	−10	4	−3	−3	−11	−0.3	−0.3	−0.3	
Kainzas	CO	199	−6	60	−158	248	−3	−5	0	−2	−9	6	−2	3	18	0.2	0.2	0.2	
CO avg			**5 ± 23**	**6 ± 23**	**7 ± 23**	**8 ± 23**	**9 ± 23**	**10 ± 23**	**11 ± 23**	**12 ± 23**	**13 ± 23**	**14 ± 23**	**15 ± 23**	**16 ± 23**	**17 ± 23**	**18 ± 23**	**19 ± 23**	**20 ± 23**	
Murchison	CM2	200	−41	46	−255	−326	−13	0	2	1	−24	−21	−23	−29	−31	0.1	0.0	0.0	
Murchison	CM2	201	−38	−29	−230	−381	−26	7	2	4	1	−14	−7	−14	−29	0.2	0.0	0.1	
Murchison	CM2	402	−7	20	−210	−1902	−15	3	−1	1	−13	−18	−16	−45	−52	0.1	0.1	0.1	
CM avg			**−29**	**12**	**−232**	**−870**	**−18**	**3**	**1**	**2 ± 3**	**−12**	**−18**	**−15 ± 4**	**−29**	**−37**	**0.1**	**0.0**	**0.1 ± 0.1**	
Chainpur	LL3.4	396	−53	5	279	348	−16	6	−1	2	−2	−4	−3	19	28	0.0	−0.1	−0.1	
Roosevelt	H3.4	398	−16	−16	−174	−76	−31	3	3	3	−31	−25	−28	28	19	0.2	−0.3	0.0	
Roosevelt	H3.4	400	−6	1	−159	−92	−24	6	3	5	−30	−21	−25	−30	−41	−0.4	−0.4	−0.4	
Ordinary C. avg			**−25**	**−3**	**−18**	**60**	**−24**	**5**	**2**	**3 ± 3**	**−21**	**−16**	**−19 ± 6**	**6**	**2**	**−0.1**	**−0.3**	**−0.2 ± 0.2**	
MAC88136	EL3	209	20	22	−245	−62	−3	3	4	4	−12	−14	−13	5	−9	0.2	0.1	0.2	
NWA 753	R3.9	199	82	10	−134	280	−17	−5	−10	−7	0	−11	−6	39	72	−2.0	−2.0	−2.0	

The reported uncertainties for single measurements (first row) represent the 2SD intermediate precision (or external reproducibility) obtained from repeated analyses of LP1 (Table 2). Uncertainties on pooled measurements are reported when at least four measurement are available and are expressed as the two-sided Student's-t 95% confidence intervals. Since ^{118}Sn, ^{119}Sn and δ^{120}Sn/^{116}Sn were measured in two cup configurations (L and H config.), both values are reported along with their average.
In the "CV selected" three measurements of CV that yielded anomalously high ^{117}Sn (see text for explanation) are excluded. The values of ^{118}Sn and ^{119}Sn are averages from measurements of two cup configurations for light (L config) and heavy (H config) masses.
"*r*" indicates a replicate measurement of the previous sample obtained from the same sample solution. δ^{116}Sn/^{120}Sn expresses the per mill variations relative to the bracketing SRM3161a. Meteorite samples were provided by Addi Bischoff – University of Münster (CV3 NWA 3118, R NWA 753, CO3 Dar al Gani 067, CV3 Acfer 082), Erik Strub – University of Cologne (LL3.4 Chainpur, H3.4 Roosevelt, CO3.8 Isna), MWG NASA (EL3 MAC 88136, CK ALH 85002), Smithsonian Institute (CM2 Murchison, CV3 Allende), Russian Academy of Science (CO3 Kainzas).
* From an analytical session that yielded anomalous ^{115}Sn data. These samples were processed using modified separation schemes (i.e. with an additional cation exchange step along with a modified anion exchange separation with Sn eluted in 1 M HNO_3 + 1 M HF). Due to the impossibility of evaluating the reasons for the anomalous data, ^{115}Sn measurements are not reported.
** From an analytical session that yielded negative (<10^{-7}) ^{113}In/^{120}Sn after correction for ^{113}Cd, hence μ ^{115}Sn data corrected for ^{115}In are not reported.

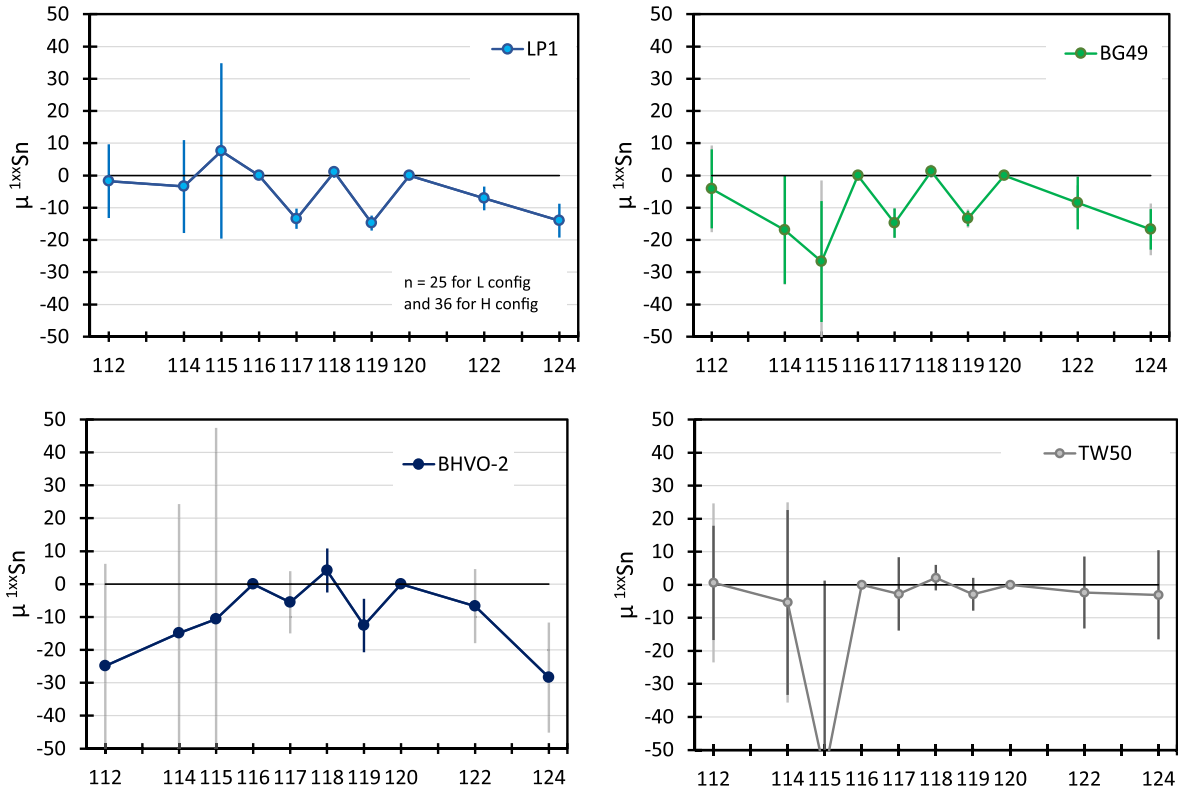

Fig. 3. Tin average isotope patterns measured in terrestrial rocks. For n (number of replicates) ≥ 4, error bars (colored and dark grey) are reported as two-sided Student's-t 95% confidence intervals. of the average of multiple measurements. For $n \leq 4$, uncertainties (light grey error bars) are calculated from the 2SD obtained from replicate measurements of LP1 (i.e., the samples with the largest number of replicates, see Table 2) divided by $\sqrt{n}$. Light grey error bars are also shown for $n \geq 4$ when they are larger than those estimated from two-sided Student's-t 95% confidence intervals. In such a case, they are displayed as light grey extension of the other error bars. Each isotope variation, expressed in the μ-notation, is normalized to ^{120}Sn. All data are corrected for instrumental mass bias, using the exponential law and normalized to ^{116}Sn/^{120}Sn = 0.4460.

(0.005–0.085 μg/g), resulting in In/Sn ratios that range between 0.01 and 0.19 (Supplementary Table S2).

4. Discussion

Replicate analyses of terrestrial and chondrite samples display variations that are characteristic for each type of sample (Fig. 3, Fig. 4). As a general feature, the offsets in μ^{117}Sn and μ^{119}Sn are similar, while variations in μ^{122}Sn are often about half of what is observed for μ^{124}Sn. Neutron capture effects, mass-dependent/independent isotope fractionation, and nucleosynthetic isotope anomalies can influence the relative abundance of Sn isotopes. Their effect and origin is discussed below. The first part of the discussion on stable isotope fractionation and nucleosynthetic isotope anomalies deals with μ^{115}Sn only marginally, because: (1) The large variations and associated measurement uncertainty make ^{115}Sn less sensitive to the processes discussed for other Sn isotopes; (2) ^{115}Sn is the only radiogenic Sn isotope owing to the decay of ^{115}In. Hence, ^{115}Sn will be treated separately afterwards.

4.1. Neutron capture effects

In theory, neutron capture could affect the relative abundance of Sn isotopes in meteorites due to the capture of secondary neutrons after exposure to cosmic rays. Among Sn isotopes, ^{115}Sn has the largest thermal neutron capture cross section (43 barn) followed by ^{119}Sn (2.2 barn) and ^{117}Sn (1.1 barn) (Mughabghab, 2018). The observed negative shifts of μ^{1xx}Sn values in meteorites roughly correlate with neutron capture cross sections. However, the absolute values of Sn neutron capture cross sections are small compared to isotopes of other elements with resolvable neutron capture effects (e.g., Leya and Masarik, 2013). For example, ^{113}Cd has a neutron capture cross section of ~20000 barn while the maximum shift observed in chondrites is <70 ppm for ^{113}Cd (Toth et al., 2020). Lunar rocks and chondrites (especially ordinary chondrites) display very similar responses to thermal and epithermal neutrons (Leya and Masarik, 2013). No neutron capture effects were detected for Sn in lunar rocks (Wang et al., 2019) although neutron capture effects are generally much larger in lunar samples than in chondrites (Lingenfelter et al., 1972; Hidaka et al., 2000b, 2000a; Sprung et al., 2013; Toth et al., 2020). Because of the above arguments, detectable neutron capture effects in chondrites are not expected for Sn isotopes.

4.2. Quantification of mass-dependent/independent processes and nucleosynthetic isotope variations

4.2.1. Nucleosynthetic isotope anomalies

Tin isotopes are synthesized in different stellar environments. As such, it is possible to calculate the expected patterns for nucleosynthetic isotope anomalies. As an example, Fig. 6A shows theoretical patterns for excesses and deficits in p-, s-, and r- process isotopes. Different estimates for the relative contribution of p-, s-, r- processes (e.g., Travaglio et al., 2004; Bisterzo et al., 2011, 2014) can result in variations in predicted nucleosynthetic patterns (e.g., Elfers et al., 2018). We prefer to use the estimates of the "main s-contribution" (Bisterzo et al., 2011), instead of that from galactic chemical evolution (e.g., Travaglio et al., 2004; Bisterzo et al., 2014) because for mid-mass range elements like Sn the later model seems to underestimate the s-process

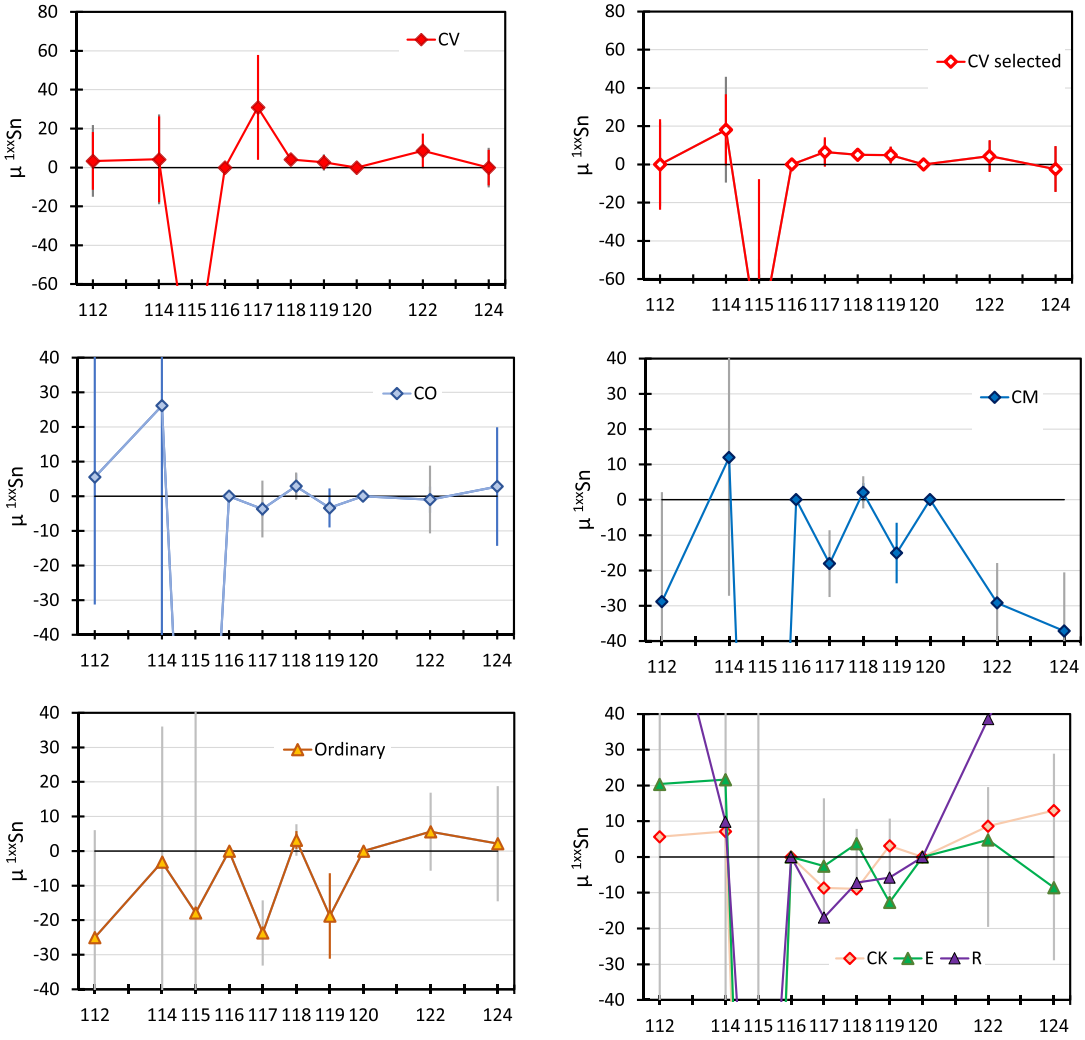

Fig. 4. Tin average isotope patterns measured in extraterrestrial materials. The pattern of "CV selected" is obtained excluding three measurements of CV that yielded anomalously high ^{117}Sn (see text for explanation). The colored error bars are reported when n ≥ 4 (CV, CO and μ^{118}Sn and μ^{119}Sn of CM and ordinary chondrites) and represent the two-sided Student's-t 95% confidence intervals of the average of multiple measurements. Grey error bars are obtained from the 2SD of repeated measurements of sample LP1 and divided by $\sqrt{n}$. Grey error bars are used for n ≤ 4 but they are also shown for n ≥ 4 when they are larger than the two-sided Student's-t 95% confidence intervals and are displayed as an extension of the colored error bars.

production of about 25% (Bisterzo et al., 2014). This is especially important for the so called "s-only isotopes" such as ^{116}Sn, which cannot be produced during r-process due to the shielding effect of ^{116}Cd. In particular, the model of Bisterzo et al. (2014) predicts only a 68% s-process contribution on ^{116}Sn, while the "main-s contribution" of Bisterzo et al. (2011) yielded 96% of the solar ^{116}Sn. Following the latter model, the remaining 4% can be ascribed to a minor p-process source due to double β^+ decay from ^{116}Te, which forms in the reaction ^{112}Sn(α, γ)^{116}Te (Özkan et al., 2007; Netterdon et al., 2015). For Sn isotopes heavier than ^{116}Sn, an r-contribution is possible and it can be calculated by subtracting the s-process contribution of Bisterzo et al. (2011). Similarly, the p-process contributions on ^{112}Sn, ^{114}Sn, and ^{115}Sn (Travaglio et al., 2011) are obtained as difference between the measured solar system abundance and that predicted by s-process. Regarding ^{115}Sn, it is debated if this nuclide forms during the p- or s-process (Dillmann et al., 2008; Hayakawa et al., 2009).

4.2.2. Mass-dependent isotope fraction (MDF) processes

The μ-values reported in Table 2, Table 3, and Supplementary Table S1 are obtained after normalization to ^{116}Sn/^{120}Sn = 0.4460 (Devillers et al., 1983) using the exponential law of Russell et al. (1978). Although not perfect, this approach is efficient in correcting the instrumental mass bias of the MC-ICP-MS (e.g., Vance and Thirlwall, 2002; Wombacher and Rehkämper, 2003), especially if deviations in the isotope compositions of samples are expressed relative to (bracketing) standards. However, the exponential law correction introduces biases if the samples are affected by MDF relative to the standard in a way that does not follow the exponential law. The exponential law is identical to the kinetic law of Young et al. (2002) and should therefore efficiently correct kinetic MDF. Equilibrium isotope partitioning follows a mass fractionation law that differs from the exponential law (Matsuhisa et al., 1978; Young et al., 2002). Thus, systematic deviations may occur if samples were affected by equilibrium MDF in nature or in the laboratory (or during the preparation of NIST SRM 3161a). In order to evaluate the effect of Sn MDF we use the generalized power law of Maréchal et al. (1999), which contains the different MDF laws (Eq. (3)):

$$\frac{r_{1xx/120}}{R_{1xx/120}} = \left(\frac{r_{116/120}}{R_{116/120}}\right)^{\theta_{gpl}} \qquad \theta_{gpl} = \frac{m^q_{120} - m^q_{1xx}}{m^q_{120} - m^q_{116}} \quad \text{Generalized Power law} \tag{3}$$

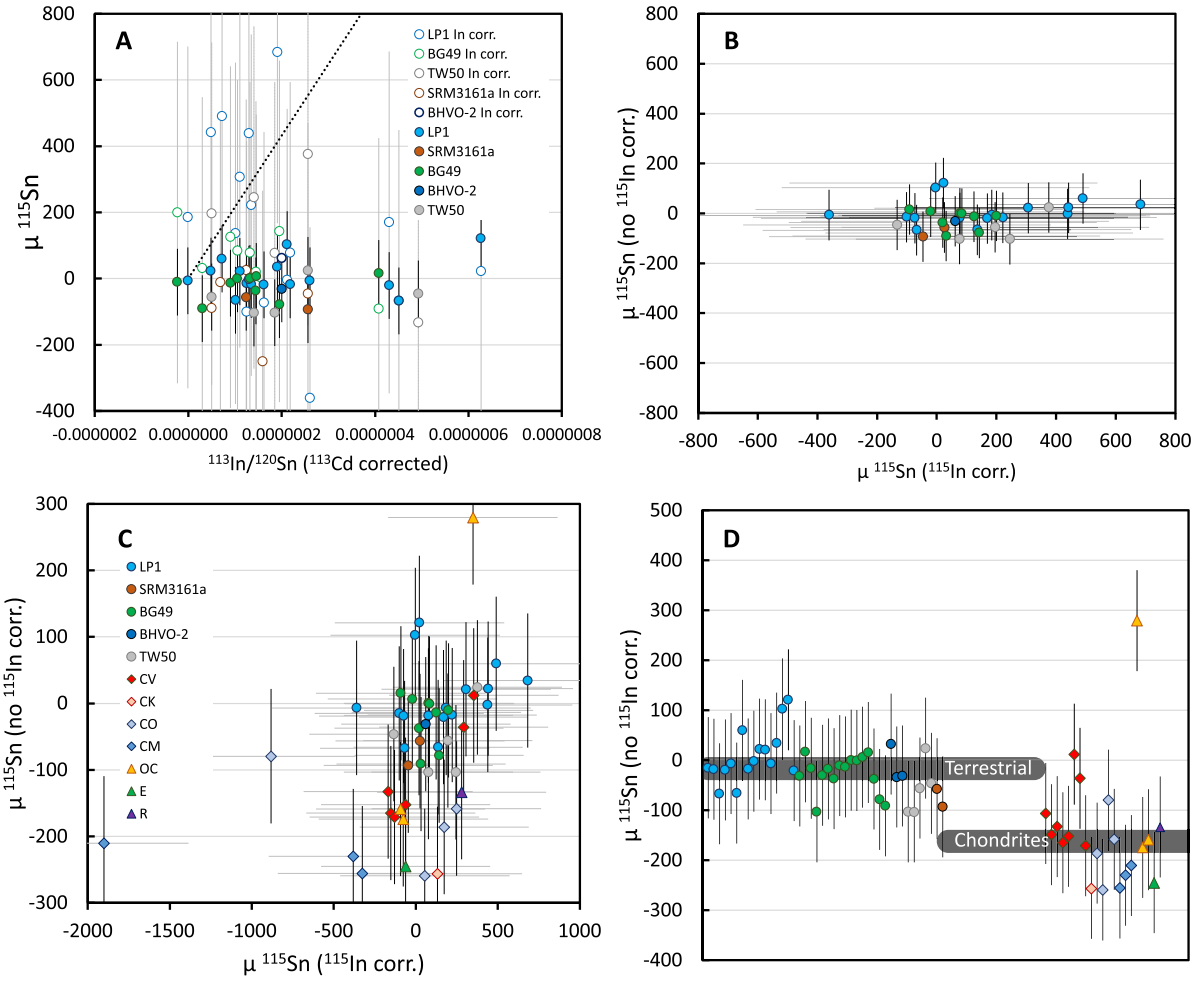

Fig. 5. Data for ^{115}Sn and evaluation of interference corrections. (A) μ^{115}Sn for terrestrial samples corrected (open symbols) and uncorrected (filled symbols) for ^{115}In isobaric interference as function of the ^{113}In/^{120}Sn ratio, which was corrected for ^{113}Cd interference on m/z 113. The dotted line represents the hypothetical trend of a sample with In-uncorrected μ^{115}Sn = 0 and affected by ^{115}In interference according to ^{113}In/^{120}Sn. The horizontal trend of In-uncorrected ^{115}Sn data (filled symbols) attests that the ^{115}In contribution is insignificant, in contrast with what estimated from ^{113}In/^{120}Sn. (B) Comparison between ^{115}Sn data corrected and uncorrected for ^{115}In isobaric interference for terrestrial samples, showing that In-corrected ^{115}Sn data result in larger scatter. (C) Comparison between ^{115}Sn data corrected and uncorrected for ^{115}In isobaric interference for terrestrial and carbonaceous (CV, CK, CO, CM), ordinary (OC), enstatite (E) and Rumuruti (R) chondrite samples. (D) ^{115}Sn data uncorrected for ^{115}In isobaric interference, showing that terrestrial samples yielded near zero μ^{115}Sn while chondrites tend towards negative values. The brown circles represent the NIST SRM 3161a solution that was processed through the chemical separation protocol.

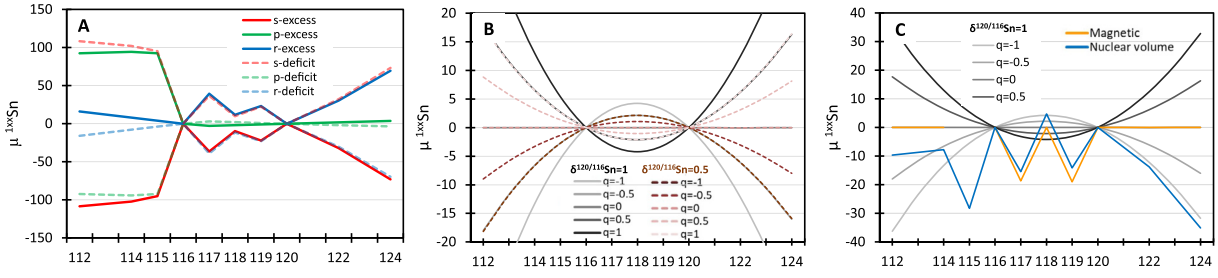

Fig. 6. Predicted Sn isotope patterns. (A) Nucleosynthetic isotope anomalies obtained by adding or removing 0.01% of s-, p-, r- process. The s-process fraction is from Bisterzo et al. (2011), while the remaining contribution is assumed to derive from p-process (^{112}Sn, ^{114}Sn, ^{115}Sn, ^{116}Sn) or r-process (^{117}Sn, ^{118}Sn, ^{119}Sn, ^{120}Sn, ^{122}Sn, ^{124}Sn), see text for details. (B) Mass-dependent isotope fractionation with $\delta^{120/116}Sn_{SRM\ 3161a}$ = +1 (grey), and +0.5 (brown–pink) for different q values (−1, −0.5, 0, 0.5, 1) for the generalized power law. (C) Stable isotope fractionation in the form of mass-dependent and mass-independent isotope fractionation. In blue, nuclear volume effect, in yellow magnetic isotope effect. Note that the magnetic isotope effect on ^{115}Sn is unknown. Nuclear charge radii are taken from Angeli and Marinova (2013). The extent of the two mass-independent isotope effects is arbitrary. In shades of grey, effects of mass-dependent isotope fractionation for different q with $\delta^{116/120}Sn_{SRM\ 3161a}$ = 1.

In the equation above, m refers to the mass of the isotopes, and q defines the MDF law (see below). Interference-only corrected isotope ratios are defined as r, R expresses isotope ratios corrected for mass fractionation with the exception of $R_{116/120}$, which is used for normalization and assumed to be 0.4460 (Devillers et al., 1983). The generalized power law is equivalent to the equilibrium law

for q = −1, the exponential law for q → 0 and the power law for q = 1 (Maréchal et al., 1999; Wombacher and Rehkämper, 2003). In the case of the exponential law, Eq. (3) becomes:

$$\frac{r_{1xx/120}}{R_{1xx/120}} = \left(\frac{r_{116/120}}{R_{116/120}}\right)^{\theta_{exp}} \quad \theta_{exp} = \frac{\ln(m_{120}/m_{1xx})}{\ln(m_{120}/m_{116})} \quad \text{Exponential law} \quad (4)$$

As stated above the exponential law does not perfectly describe the instrumental mass discrimination (Vance and Thirlwall, 2002; Wombacher and Rehkämper, 2003). In addition, another potential source of inaccuracy is represented by the assumed $^{116}Sn/^{120}Sn$ reference value. These two issues can influence the mass bias correction and the resulting $R_{1xx/120}$. However, $\mu^{1xx}Sn$ are little affected by these approximations because similar biases are expected for both samples and bracketing standards.

Fig. 6B (and Fig. 6C) shows the expected $\mu^{1xx}Sn$ for samples that display MDF relative to the NIST SRM 3161a. The curves are obtained for variable q (i.e., different MDF laws) and $\delta^{116/120}Sn_{SRM\ 3161a}$, which expresses the extent of the stable isotope fractionation. They were calculated as follows: first, the initial isotope composition, which is assumed to be identical to that of NIST SRM 3161a (i.e., $\delta^{120/116}Sn_{SRM\ 3161a} = 0$ and $\mu^{1xx}Sn = 0$ per definition) was biased to mimic an arbitrary mass-dependent isotope fractionation (i.e., $\delta^{120/116}Sn_{SRM\ 3161a} = 0.5$ or 1) using the generalized power law with variable q-values. Second, the obtained isotope composition was re-normalized to $\delta^{116/120}Sn_{SRM\ 3161a} = 0$ using the exponential law to mimic the instrumental mass fractionation correction. The calculated $\mu^{1xx}Sn$ patterns (Fig. 6B) have parabolic shapes, with larger deviations for the lightest and heaviest isotopes. As shown in Fig. 6B, the same deviations are obtained at constant $q \times \delta^{120/116}Sn_{SRM\ 3161a}$. For MDF in the per mil range, μ values can shift up to tens of ppm. For instance, in the case of equilibrium isotope fractionation ($q = -1$), a $\delta^{120/116}Sn_{SRM\ 3161a} = 1$ shifts results in offsets of −36 and −32 ppm for $\mu^{112}Sn$ and $\mu^{124}Sn$, respectively. Therefore, MDF can significantly affect high precision measurements of Sn isotopes, provided that per mil level isotope fractionation occurred with non-exponential law mass-fractionation behavior. Without further evaluation, we like to note, that reduced and molecular, rather than atomic, masses may apply for some kinetic isotope fractionation processes (Young et al., 2002), which can also lead to apparent isotope anomalies. Mass-dependent variations larger than 1‰ (for $^{120}Sn/^{116}Sn$) have been reported for chondrites and mantle derived rocks (e.g., Wang et al., 2018; Creech and Moynier, 2019; Wang et al., 2021b), emphasizing that the effect of stable isotope fractionation cannot be neglected when looking on nucleosynthetic anomalies at the ppm level. The parabolic curves constructed in Fig. 6B and C, based on the generalized power law, provide a basis for recognizing these effects.

4.2.3. Mass-independent isotope fractionation (MIF): nuclear volume and magnetic isotope effects

The correlated odd isotope offsets for $\mu^{117}Sn$ and $\mu^{119}Sn$ point to MIF processes. Two physical processes are candidates for the fractionation of odd isotopes from even ones: the nuclear volume effect and the magnetic isotope effect (see e.g., Dauphas and Schauble, 2016 for a review). Owing to its isotope configuration, Sn allows to discriminate analytically between the two MIF processes. To do so, it is necessary to quantitatively model the patterns predicted by the two MIF processes. This can be easily accomplished for the magnetic isotope effect as it affects only the odd isotopes to a similar extent (Malinovskiy et al., 2009). Thus, it results only in comparable variations for $\mu^{117}Sn$ and $\mu^{119}Sn$ (Fig. 6C). The nuclear volume effect can be modelled using the mean-squared radii $\delta < r^2 >$ of each nuclide and normalizing to $^{116}Sn/^{120}Sn$ (c.f. Fujii et al., 2006). The so calculated nuclear volume effect predicts $\mu^{117}Sn \approx \mu^{119}Sn \approx \mu^{122}Sn \approx 0.5 \times \mu^{124}Sn$ (Fig. 6C). As shown in Fig. 6A and C, an s-process excess results in an isotope pattern that is very similar to that of a nuclear volume effect, with the exception of the two lightest isotopes, ^{112}Sn and ^{114}Sn. These two p-process isotopes show the largest depletion following an s-process variation, whereas they are less affected by nuclear volume effects in comparison to other isotopes.

4.3. Natural vs laboratory origin of mass-dependent and mass-independent isotope fractionation

Isotope variations triggered by MDF or MIF can occur in the laboratory, during the chemical preparation or mass spectrometry. Mass-dependent isotope fractionation related to the preparation of the samples in the laboratory, is likely more pronounced at lower recovery of the analyte. In Supplementary Fig. S5, $\delta^{120/116}Sn_{SRM\ 3161a}$ are plotted against the procedural yield. Even if the scatter is large, for same of the measurements it is possible to hypothesize a shift towards light $\delta^{120/116}Sn_{SRM\ 3161a}$ at low (<70%) procedural yield. This suggests that heavy Sn isotopes might be preferentially lost during sample treatment. However, mass bias corrected data do not show significant variations with the procedural yield (as shown for $\mu^{124}Sn$ in Supplementary Fig. S5) suggesting that, if MDF is induced in the laboratory, this is efficiently corrected with the exponential law. Considering also that only three chondrites had procedural yields <70% (between 65 and 70%), it seems unlikely that $\mu^{1xx}Sn$ data are significantly affected by MDF induced during sample treatment.

Chemically induced MIF for Sn was observed in photochemical reactions (Malinovskiy et al., 2009) and liquid–liquid extraction experiments with a crown ether (Moynier et al., 2009b). It is therefore plausible that similar isotope fractionation effects occurred during the sample treatment in the laboratory prior to MC-ICP-MS measurements. However, this hypothesis is in contrast with several observations: (i) MIF effects are not clearly resolvable for NIST SRM 3161a processed through ion exchange columns, (ii) the observed variations depend on sample type and they are reproducible for repeated digestions, (iii) laboratory induced mass-independent fractionation is expected to be larger for lower recovery of the analyte, but there is no correlation between procedural yields and MIF (Supplementary Fig. S5).

Mass-independent isotope fractionation, mostly in the form of magnetic isotope effects, can also be produced during MC-ICP-MS analyses (e.g., Shirai and Humayun, 2011; Yang et al., 2018 for a review). Some observations based on previous studies might suggest that similar processes can also occur for Sn. Wang et al. (2017) used a set up that is similar to ours, operating a Thermo Scientific Neptune with an Aridus II. The authors did not report ^{119}Sn data due to analytical issues, which were interpreted as consequences of unknown polyatomic interferences. Mass-independent effects could represent an alternative source for erratic ^{119}Sn. In this case, a similar effect would be expected for ^{117}Sn. The authors did not describe problems with ^{117}Sn but this isotope was added with their double spike, making it difficult to distinguish small variations. Friebel et al. (2020) observed drifts in $^{117}Sn/^{120}Sn$ and $^{119}Sn/^{120}Sn$ during analytical sessions with a Nu Plasma II MC-ICP-MS combined to a DSN 100 desolvator. The authors proposed variable MIF as an explanation. Therefore, in principle, non-zero μ values in MC-ICP-MS Sn measurements could also reflect variations of plasma conditions between samples and the NIST SRM 3161a bracketing solution.

The presence of matrix elements imperfectly separated from the analyte could trigger MIF or MDF variations between NIST SRM 3161a bracketing solution and sample measurements. The possible occurrence of matrix effects could originate from an

incomplete purification of Sn from other elements. To investigate this hypothesis, the purified Sn solutions were analyzed with a Thermo Scientific iCAP ICP-MS in search of possible impurities, using a set up similar to that adopted for testing Sn recovery (See Supplementary material). These analyses did not detect significant contamination of a specific element (analyzed elements were: Be, Na, Mg, Al, K, Ca, Sc, Ti, V, Cr, Mn, Fe, Co, Ni, Cu, Zn, Ga, Rb, Sr, Y, Zr, Nb, Mo, Pd, Cd, In, Cs, Ba, La, Nd, Ho, Hf, Ta, W, Ir, Tl, Pb, Bi, Th, U). Moreover, if impurities are responsible for MDF or MIF during MC-ICP-MS, one may expect variations as a function of the amount of digested sample. This is because if the columns resulted in imperfect separation of one element, this effect is expected to change at variable sample load (and slightly variable chemical procedure). As shown in Supplementary Fig. S5, there is no correlation between μ^{119}Sn or μ^{124}Sn and the amount of processed powder. In addition, also organic matter stripped from the resin can trigger MIF (e.g., Pietruszka and Reznik, 2008 for Mo). However, this possibility appears unlikely in our case because "doped blank" tests (i.e. the Sn NIST SRM 3161a standard mixed with a solution that had been collected after the Sn separation procedure) show no significant shifts in μ^{1xx}Sn values (Supplementary Table S1 and Fig. S4). Most importantly, since chondrites have a rather similar chemical composition, it is difficult to explain characteristic isotope fractionation patterns of different chondrite groups with a laboratory origin. Therefore, a geo-cosmochemical origin seems the most viable explanation for the observed variations in μ^{117}Sn, μ^{119}Sn, μ^{122}Sn, and μ^{124}Sn. Certainly, further high precision studies are required to address this issue.

4.4. Isotope fractionation in terrestrial samples and chondrites

4.4.1. Terrestrial samples

The correct identification of MDF and MIF effects relies on the basic assumption that the NIST SRM3161a is sufficiently representative of the unfractionated starting material. This assumption seems reasonable as the estimated BSE composition ($\delta^{120/116}Sn_{SRM\ 3161a}$ = −0.04 ± 0.06) is close to that of NIST SRM3161a (Wang et al., 2018). The three terrestrial basalts (LP1, BG49, BHVO-2) show similar patterns, characterized by average negative μ values for ^{117}Sn, ^{119}Sn, ^{122}Sn, ^{124}Sn (Fig. 3). The similarly negative μ^{117}Sn and μ^{119}Sn of LP1 and BG49 clearly indicate the occurrence of MIF effects. The pattern for even Sn isotopes is qualitatively consistent with heavy isotope enrichment in melts due to the more incompatible behavior of Sn^{4+} during partial mantle melting (Wang et al., 2018). This is caused by both mass-dependent equilibrium isotope partitioning and nuclear volume effects. A nuclear volume effect could be also responsible for the shift in the odd isotopes μ^{117}Sn and μ^{119}Sn. However, relative to μ^{122}Sn and μ^{124}Sn, the offset in μ^{117}Sn and μ^{119}Sn is too large for a nuclear volume effect alone. Therefore, the shift in μ^{117}Sn and μ^{119}Sn rather suggests the presence of a magnetic isotope effect. The negative μ^{122}Sn and μ^{124}Sn is either explained by additional nuclear volume effects or equilibrium MDF. The second possibility can be tested modeling MDF processes as described above. Using the generalized power law and the lowest reasonable value $q = -1$ (equilibrium isotope fractionation), sufficient shifts in μ^{122}Sn and μ^{124}Sn are obtained only for $\delta^{120/116}Sn_{SRM\ 3161a} \geq +0.5‰$ (Fig. 7). Our measured $\delta^{120/116}Sn_{SRM}$

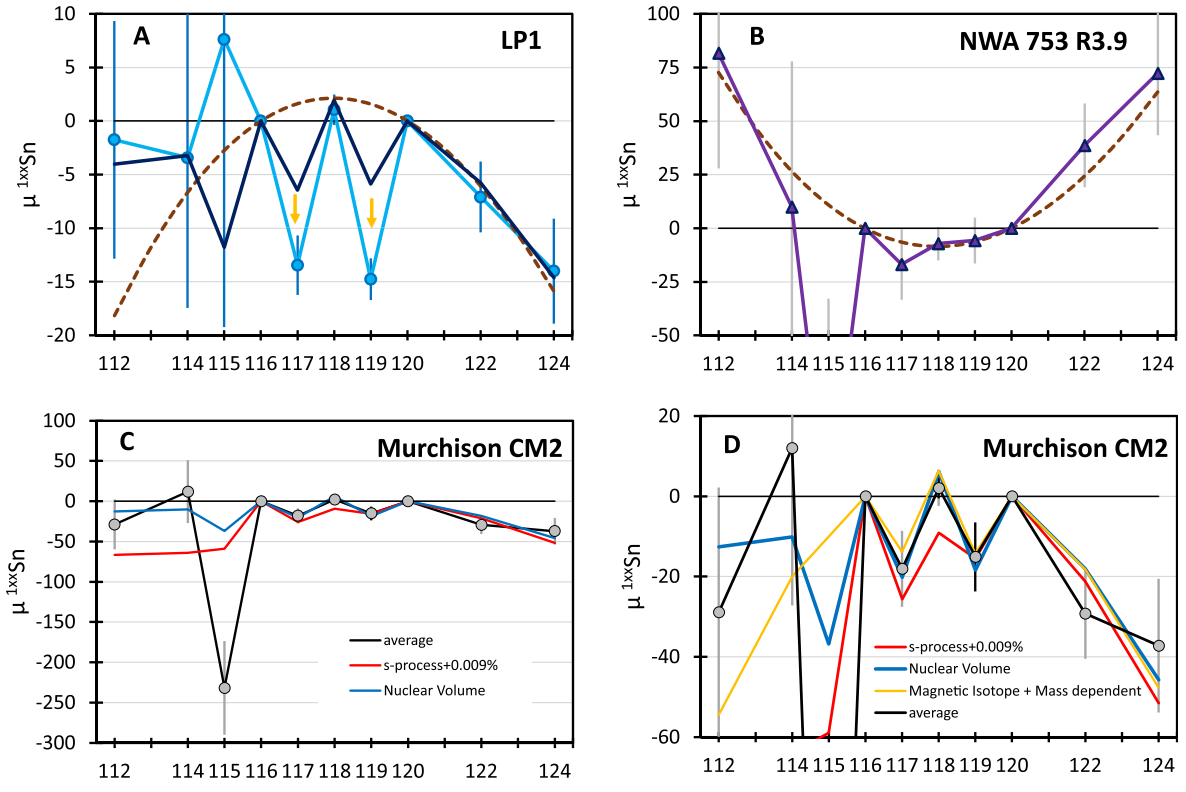

Fig. 7. Comparison between measured and modelled isotope patterns. (A) Average pattern of sample LP1 (in light blue) in comparison to different theoretical isotope fractionation processes: In brown (dashed line) mass-dependent isotope fractionation modelled following the GPL and using $\delta^{120/116}Sn_{SRM\ 3161a}$ = 0.5‰ and q = −1; in dark blue nuclear volume effect; yellow arrows indicate a contribution from the magnetic isotope effect, which influences only the odd isotopes. (B) In purple the measured isotopic pattern of NWA 753 R3.9. In dashed brown, the calculated effect of mass-dependent equilibrium isotope fractionation (generalized power law with q = −1 and $\delta^{120/116}Sn_{SRM\ 3161a}$ = −2.0‰), which corresponds to the offset in ^{120}Sn/^{116}Sn between the bracketing solution and the sample during the analytical session (Table 3). (C and D) Average pattern of Murchison CM2 (in black).. The red line reproduces the calculated pattern for an s-process excess of 0.009%. In blue, the theoretical pattern expected for a nuclear volume effect. In yellow, the combination of a magnetic isotope effect with a mass-dependent isotope fractionation assuming $\delta^{120/116}Sn_{SRM\ 3161a}$ = 1.5‰ and q = −1. Error bars as in Figs. 3 and 4: colored (LP1) and dark grey (CM2 Murchison) error bars represent the two-sided Student's-t 95% confidence intervals; light grey error bars are estimated from repeated measurements of sample LP1 as $2SD/\sqrt{n}$, where n is the number of measurements.

$_{3161a}$ in terrestrial basalts varies between –1.1 ± 0.6‰ and +0.6 ± 0.6‰, with an average of 0.2‰, generally lower than what is expected for this scenario. Moreover, $\delta^{120/116}Sn_{SRM\ 3161a} \geq +0.5$‰ is significantly higher than what is observed in the literature. Basalts of Wang et al. (2018) show $\delta^{120/116}Sn_{SRM\ 3161a} \leq +0.14$ (as recalculated from their $\delta^{124/116}Sn_{SRM\ 3161a}$ notation) and stronger isotope fractionation would require an unrealistic pyroxenite-rich source (Wang et al., 2018). Values of $q > -1$, require even higher $\delta^{120/160}Sn_{SRM\ 3161a}$ to fit the measured μ^{122}Sn and μ^{124}Sn. Additional evidence against significant MDF fractionation in LP1 and BG49 is represented by their μ^{112}Sn and μ^{114}Sn because they do not show a significant shift towards negative values (Fig. 2 and Fig. 7). In contrast, the modeled nuclear volume effect fits the data, including ^{112}Sn and ^{114}Sn (Fig. 7). Although only few measurements are available for BHVO-2, it shows negative μ^{124}Sn and possibly μ^{112}Sn and μ^{114}Sn (although not statistically resolvable), which could indicate MDF. Wang et al. (2017) reported $\delta^{120/116}Sn_{SRM\ 3161a} = -0.13$‰ for BHVO-2, which could only reproduce our data with an unrealistically low value of $q = -5$. Friebel et al. (2020) also measured BHVO-2, with uncertainties similar to ours but reported no evidence for significant differences from the bracketing NIST SRM 3161a. Therefore, the overall Sn isotope signature of BHVO-2 remains ambiguous, but it should be stressed that only three replicates were determined for BHVO-2 and the average μ offsets are only slightly larger than the analytical uncertainty. In conclusion, the patterns of basaltic samples suggest the presence of ppm-level mass-independent processes as a combination of magnetic isotope and nuclear volume effects. Mass-dependent processes are also likely (Wang et al., 2017, 2018; Badullovich et al., 2017) but cannot be clearly identified with our dataset.

4.4.2. Ordinary chondrites

Ordinary chondrites display the largest anomalies in μ^{117}Sn and μ^{119}Sn (although μ^{119}Sn of Chainpur overlaps with zero), but display no significant deviations from the NIST SRM 3161a bracketing solution in μ^{122}Sn and μ^{124}Sn (Fig. 4). Therefore, their pattern suggests the presence of MIF due to the magnetic isotope effect.

4.4.3. CV, CO, CK chondrites

Carbonaceous chondrites show variable μ^{117}Sn and μ^{119}Sn (Fig. 4). Three CV (two digestions of Allende and one of NWA 3118) resulted in very high μ^{117}Sn (up to 85 ± 16) (Tab 3, Fig. 4). Other aliquots of Allende and the Acfer 082 CV3 chondrite do not show such high μ^{117}Sn. These excesses in μ^{117}Sn cannot be explained by nucleosynthetic, or stable isotope fractionation processes. An analytical artefact seems also unlikely because there is no record of similar values in terrestrial samples or in other meteorite groups. Thus, the origin of the three high μ^{117}Sn values remains unclear. When the three anomalous μ^{117}Sn values are not considered, CV chondrites show no significant anomalies due to MDF or MIF. The average CO chondrite pattern (three samples) lacks clear evidence of anomalies, similar to CV chondrites. However, CO chondrites show a tendency towards negative μ^{117}Sn and μ^{119}Sn (Fig. 4). Although differences are not statistically resolvable, the complementary odd isotope pattern between CO and CV chondrites hints towards a small fractionation in the opposite direction due to the magnetic isotope effect. The only measured CK chondrite does not show a pattern with clear sign of isotope fractionation.

4.4.4. CM chondrite

Murchison, the only processed CM chondrite, displays a strongly fractionated isotope pattern (Fig. 4). The relative deviations in μ^{117}Sn, μ^{119}Sn, μ^{122}Sn, and μ^{124}Sn are roughly consistent with either an s-process excess (0.009%) or MIF (Fig. 7). However, the nucleosynthetic model predicts negative μ^{112}Sn and μ^{114}Sn (<−60 ppm), which is not observed in the data. The mismatch could be solved by adding a small p-process component. This scenario is also equivalent to a deficit in r- and p-process components, with the latter one being less depleted. Hence, an "ad hoc" proportion of p-, s-, and r- processes can explain the pattern of Murchison. Alternatively, different combinations of MIF (and MDF) can also reproduce the pattern of Murchison. The relative shifts in μ-values are consistent with a pure nuclear volume effect (Fig. 7) or with magnetic isotope effects in combination with an additional MDF. Nucleosynthetic isotope anomalies, MDF, and MIF (both nuclear volume and magnetic isotope effects) can be distinguished based on ^{118}Sn. Mass-dependent and independent isotope fractionation predicts a small positive shift, whereas an s-process excess requires a negative μ^{118}Sn shift. The difference between the two models is only about 15 μ^{118}Sn (Fig. 7) but likely resolvable. The six replicate measurements of μ^{118}Sn of Murchison (based on three different digestions measured in both H and L configurations) yielded 2 ± 3. The three ppm uncertainty is very small and likely biased by the small number of replicates as attested by the theoretical uncertanty expected for six measurements as calculated from the multiple measurements of LP1. As such the intermediate precision on six replicates, based on replicates of LP1, is $11/\sqrt{6} = 4$ (Fig. 7). Taking an uncertanty of four ppm, the average μ^{118}Sn value of +2 is consistent with the predicted MIF model (+6), but outside the expected value for a nucleosynthetic anomaly (−9). In addition, the relative proportions between μ^{117}Sn and μ^{119}Sn is best reproduced by MIF (Fig. 7). Hence, we can reasonably conclude that the isotope signature of Murchison is better explained by MIF instead of nucleosynthetic isotope anomalies. In theory, ^{112}Sn and ^{114}Sn can be used to better constrain the MIF process (i.e., between a nuclear volume effect and a magnetic isotope effect combined with residual MDF, Fig. 7). However, this is not possible due to the large analytical uncertainties (Fig. 7). Nevertheless, to reproduce the even isotope pattern of Murchison, a MDF variation requires $\delta^{120/116}Sn_{SRM\ 3161a} = 1.5$‰ for $q = -1$ (equilibrium isotope fractionation) and even more positive $\delta^{116/120}Sn_{SRM\ 3161a}$ for higher q. Since such a large negative shift is not observed in our dataset (Table 3) and is also not reported in the literature (Creech and Moynier, 2019; Wang et al., 2021b), we can conclude that the pattern observed in Murchison corresponds to MIF, most likely in the form of a nuclear volume effect.

4.4.5. Enstatite (MAC88136) and Rumuruti (NWA 753) chondrite

The single analysis for the only investigated enstatite chondrite (EL3 – MAC88136), does not display resolvable shifts from the reference NIST SRM 3161a standard. The Rumuruti chondrite NWA 753 has a very fractionated pattern with strong positive μ-values in heavy and light isotopes. This pattern is consistent with MDF, whereby the lack of odd/even isotope anomalies may suggest that MIF was not significant. Therefore, the respective isotope fractionation process probably did not involve oxidation/reduction as nuclear volume effects would likely be expected. Relative to the bracketing standard NIST SRM 3161a, the two measurements of NWA 753 (L and H sequences), yielded $\delta^{120/116}Sn_{SRM\ 3161a} = -2.0 \pm 0.6$‰, which is the largest shift recorded among the measured samples. The calculated curve for a MDF correction with $\delta^{120/116}Sn_{SRM\ 3161a} = -2.0$‰ and $q = -1$ (equilibrium isotope fractionation) agrees precisely with the pattern observed for NWA 753 (Fig. 7). Thus, the measured isotope signature of NWA 753 is dominated by equilibrium MDF and on the low end of the range reported for chondrites (lowest offset in $\delta^{122/118}Sn$ of chondrites relative to BSE is −1.6‰, Creech and Moynier 2019), although R chondrites were not analyzed by Creech and Moynier (2019) and Wang et al. (2021b). Due to the lack of additional constrain from the literature and because the peculiar pattern of NWA 753 was observed

only in this sample, it is difficult to argue on its origin, which could reflect geo/cosmochemical processes but also processes induced during the sample treatment.

4.5. The significance of lacking Sn nucleosynthetic isotope anomalies

At the bulk meteorite scale, nucleosynthetic isotope anomalies for mid-mass range elements occur as s-process deficits relative to Earth (e.g., Dauphas et al., 2002; Chen et al., 2010; Qin et al., 2011; Burkhardt et al., 2012a; Akram et al., 2015; Fischer-Gödde et al., 2015; Ek et al., 2020). The largest variations are reported for refractory elements with intermediate masses (e.g., Cr, Ti, Qin and Carlson, 2016), suggesting that the occurrence of anomalies depends on the atomic number and the volatility of the element. During stellar nucleosynthesis, Sn nuclides are produced between the light s-process peak around the magic neutron number 50 (e.g., ^{92}Zr) and the heavy s-process peak at the magic neutron number 82 (e.g., ^{136}Xe) (Bisterzo et al., 2010). The atomic region 50 < A < 82 includes refractory elements (i.e. Zr, Mo, Ru), moderately volatile elements (Ag, Cd, Sn and Te), Pd as a slightly volatile element, and the noble gas Xe. Refractory elements of this mass region display the largest deficit in s-process nuclides at the bulk meteorite scale, while heavier refractory elements show smaller or no anomalies. The mass-dependence of s-process anomalies for similarly refractory elements was explained involving a specific s-process component, heterogeneously distributed in the solar system. This component originated from a nucleosynthetic environment that produced mainly mid mass elements. The source of this component was identified as AGB stars with high metallicities (Ek et al., 2020; Lugaro et al., 2020). In such stellar environments, the production of Sn nuclides is related to an intermediate s-process peak (Bisterzo et al., 2010). As such, the lack of Sn nucleosynthetic anomalies cannot be explained by stellar production scenarios. Instead, it must reflect later processes that discriminated between refractory and volatile elements since all the investigated moderately volatile elements (Se, Cd, Sn, Te) show a homogeneous nucleosynthetic signature among different chondrite groups (Fehr et al., 2006; Labidi et al., 2018; Toth et al., 2020). Acid leachates and residues of chondrites reveal even more pronounced nucleosynthetic isotope anomalies for the refractory elements Zr and Mo (e.g. Schönbächler et al., 2005; Burkhardt et al., 2012b; Elfers et al., 2020). In contrast, the nucleosynthetic signature of the moderately volatile elements Cd and Te are (almost) homogeneous within chondrites (Fukami and Yokoyama, 2017; Toth et al., 2020). This strongly suggests that no or negligible amounts of moderately volatile elements characterized by nucleosynthetic isotope anomalies are locked up in presolar phases. The absence of isotope anomalies is therefore clearly linked to elemental volatilities (Fehr et al., 2006; Wombacher et al., 2008; Fukami and Yokoyama, 2017). Potentially, volatile elements could have been lost from the presolar phases upon heating in the solar nebula (Fukami and Yokoyama, 2017) or on parent bodies. However, selective volatile element loss from presolar phases is unlikely because (1) volatile element loss from presolar grains may homogenize volatile elements locally, but it is unlikely that it erased solar system wide heterogeneities, and (2) the abundance of moderately volatile elements with 50% Tc between 800 and 500 K (e.g., Cd, Sn and Te) correlates with the abundance of carbonaceous chondrite matrices and nucleosynthetic isotope anomalies (Braukmüller et al., 2018; Alexander, 2019; Hellmann et al., 2020). Although these relationships may be more complex in detail, it appears inconceivable that moderately volatile elements were preferentially lost from presolar grains hosted in the matrix without volatile element loss from other chondrite phases.

If moderately volatile elements were not selectively lost from presolar phases within the protoplanetary disk or parent bodies, they probably never condensed into acid resistant presolar grains (Fehr et al., 2006; Ek et al., 2020). This scenario is in line with observations and calculations from REE in presolar SiC (Lodders and Fegley, 1997; Yin et al., 2006; Ireland et al., 2018). In this regard, Ek et al. (2020) demonstrated that nucleosynthetic isotope anomalies due to variable s-process deficits in iron meteorites relative to Earth are smaller for Pd, a slightly volatile element (50% Tc = 1324 K; Lodders 2003) than for the refractory elements Mo and Ru. As a consequence, s-process nuclides of Pd in presolar phases are 3–4 times less abundant than expected for a nucleosynthetic contribution estimated from refractory elements Mo, Ru and Zr. As the s-process yields in the Zr-Mo-Ru-Pd-Cd mass region are not substantially affected by the mass and metallicity of the parental AGB stars or variations in the ^{22}Ne neutron source, Ek et al. (2020) suggested that Pd, unlike Zr, Ru and Mo, condensed only partially into the presolar phases that formed next to AGB stars. The remaining Pd stayed in the ISM gas phase or condensed into less resistant volatile element rich dust that did not survive within the ISM (Tielens, 2005; Ek et al., 2020). Either way, as moderately volatile element nuclides from AGB sources are not locked up in resistant refractory presolar phases, their isotope compositions become homogenized within the ISM gas phase. Hence, pronounced nucleosynthetic anomalies must be absent for Sn and other moderately volatile elements (Ek et al., 2020; Toth et al., 2020).

The observation, that noble gases like Xe and Kr display nucleosynthetic isotope anomalies in presolar SiC and graphite (Lewis et al., 1990, 1994; Ott, 1993; Amari et al., 1995) appears at odds with the observation that volatile elements are absent in presolar grains. However, noble gases do not condense into presolar phases but enter them by ion implantation (Verchovsky et al., 2003). Ion implantation is also expected for reactive elements (Verchovsky et al., 2004) including moderately volatile elements. The lack of Sn nucleosynthetic anomalies implies that the effect of ion implantation for these elements is too low to be detected. Most likely this is due to the fact that Sn is much less depleted than Xe in bulk meteorites (e.g., Ott, 2014).

4.6. The ^{115}In-^{115}Sn decay system

Friebel et al. (2020) suggests that the NIST SRM 3161a standard solution contains In impurities, which can affect ^{115}Sn measurements. This was proposed on the basis of two analyses of NIST SRM 3161a solution processed through the chemistry, which resulted in lower ^{115}Sn/^{120}Sn relative to similar unprocessed solutions. This is consistent with the two tests that were performed in a similar matter (Supplementary Table S1), which also resulted in negative μ^{115}Sn (between −57 and −93 ± 101). However, it is not possible to quantify the In mass fraction in the NIST SRM 3161a standard solution due to the limited data and the analytical scatter. The current lots of NIST SRM 3161a are made by NIST from the SRM 741 Sn pure metal. After an inquiry, NIST made us aware that such material was analyzed with NAA, resulting in ~0.11 μg/g of In. This mass fraction can be used to estimate the significance of the ^{115}In interference for NIST SRM 3161a. An In/Sn ratio of 1.1×10^{-7} (g/g) corresponds to a molar ^{115}In/^{120}Sn of 3.2×10^{-7} or ^{115}In/^{115}Sn of 3.1×10^{-5}. Thus, assuming the same transmission for In and Sn during MC-ICP-MS measurements, a shift of ~31 μ^{115}Sn can be ascribed to In impurities. The contribution of the In impurity to μ^{115}Sn will probably be somewhat larger due to the lower first ionization potential of In (5.8 eV) relative to Sn (7.3 eV), and possibly due to additional In impurities introduced during the preparation of the NIST SRM 3161a from the SRM 741. Therefore, a shift in ^{115}Sn/^{120}Sn of a few tens of ppm can explain the tendency towards negative μ^{115}Sn in chemically processed NIST SRM 3161a, suggesting a systematic bias towards

higher values, which affects terrestrial and extraterrestrial sample data. However, such a shift is likely within uncertainty (i.e. ± 101 μ). Moreover as the bias is systematic, it affects only the absolute μ^{115}Sn values, but not the relative variations between samples. Hence, it does not have any effect on the following discussion of the data.

Despite the analytical difficulties for accurate ^{115}Sn/^{120}Sn measurements, the data indicate resolvable variations between terrestrial and chondritic samples. The terrestrial materials analyzed in this study, which consist of three intraplate basalts (LP1, BG49, BHVO-2) and one sedimentary rock (shale TW50), do not display significant differences between each other, and they scatter between −100 and +100 μ^{115}Sn. In contrast, most of the chondrites plot between −300 and −100 μ^{115}Sn. As such, a systematic difference in ^{115}Sn/^{120}Sn of about 150–200 ppm is observed between the terrestrial and chondritic samples (Fig. 5D). Since other Sn isotopes do not show similar systematic offsets between chondrites and terrestrial materials (Figs. 3 and 4), the μ^{115}Sn variations cannot be explained by nucleosynthetic anomalies or stable isotope fractionation (mass-dependent or mass-independent). Instead, they must reflect differences in the radioactive ingrowth of ^{115}Sn due to the β^- decay of ^{115}In, which has a half-life of 4.41 × 10^{14} a (Pfeiffer et al., 1979). The ^{115}In-^{115}Sn decay system was already described as a potential tool for dating sulfide mineralizations (Yi et al., 1995) but ^{115}Sn/^{120}Sn variations were never observed before. Due to the very long half-life, measurable differences in ^{115}Sn/^{120}Sn are only expected between reservoirs with very different time-integrated In/Sn.

In order to better constrain the In-Sn decay system, chondritic μ^{115}Sn data can be plotted against their ^{115}In/^{120}Sn ratios (Supplementary Table S2) in an isochron diagram. In such a diagram (Fig. 8), most of the chondrite data show negative μ^{115}Sn and low ^{115}In/^{120}Sn. The corresponding In/Sn ratios (0.01–0.06) are similar to literature values for carbonaceous chondrites (e.g., the In/Sn of CI is 0.05, Palme et al., 2014; Braukmüller et al., 2018). Only the ordinary chondrite Chainpur shows a much higher In/Sn of 0.19 (^{115}In/^{120}Sn = 0.57), which is also associated with high μ^{115}Sn (+279). When compared to other chondrites, the signature of this sample is consistent with the radioactive decay of ^{115}In over the age of the solar system (Fig. 8). As such, the spread observed in chondrites (and dominated by Chainpur) is roughly consistent with a 4.55 Ga isochron. It should be noted that some of the chondrites

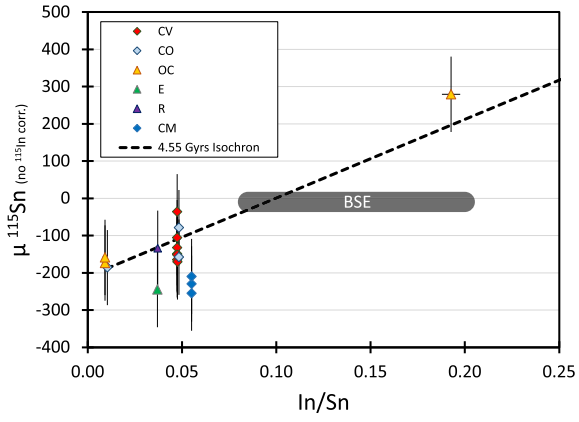

Fig. 8. ^{115}In-^{115}Sn isochron diagram. The grey field represents the estimate of the BSE composition inferred from ^{115}Sn data of the measured basalts and In-Sn mass fractions estimates from the literature (Jochum et al., 1993, Witt-Eickschen et al., 2009, Wang et al., 2016). The dashed line is a reference 4.55 Ga isochron calculated using a half-life of 4.41 × 10^{14} years (Pfeiffer et al., 1979). Most chondrite data plot along the reference 4.55 Ga isochron. The uncertainty on single μ^{115}Sn measurements is ±101 (the 2SD from multiple analyses of sample LP1; see Table 2 and 3).

are not perfecty aligned on a reference 4.55 Ga isochron as enstatite chondrite MAC88136 and CM2 Murchison fall slightly below the isochron. Reasons for this are unclear but cannot be easily explained by ^{115}In interferences during measurements (it would shift the data towards higher μ^{115}Sn) or MIF (variations are too large and do not correlate with μ^{117}Sn or μ^{119}Sn). The high In/Sn and μ^{115}Sn of Chainpur suggests that In-Sn fractionation occurred during an early stage of the solar system, likely during thermal metamorphism of the parent body (e.g., Wombacher et al., 2008), excluding any recent events (e.g., terrestrial alteration). In particular, In-Sn redistribution in the parent body of ordinary chondrites could reflect preferential evaporation/condensation due to the different volatility of the two elements. As such, the In-Sn decay system can be used to better discriminate and date processes that fractionated In and Sn long ago.

The offset in μ^{115}Sn between terrestrial samples and chondrites allows us to constrain the In-Sn budget of the silicate Earth. As a first approximation, the three measured young (<25 Myr) intraplate basalts can be considered as representative of the present-day bulk silicate Earth (BSE) in terms of μ^{115}Sn. Therefore, the BSE can be added on the In-Sn isochron diagram (Fig. 8) along with its In/Sn ratio. There are different estimates of the In and Sn mass fractionation of the BSE. For Sn, they vary between 91 (Witt-Eickschen et al., 2009) and 140 ng/g (Jochum et al., 1993), and for In between 12 (Wang et al., 2016) and 18 ng/g (Witt-Eickschen et al., 2009), resulting in calculated In/Sn_{BSE} between 0.09 and 0.20. This range is plotted as ^{115}In/$^{120}Sn_{BSE}$ in Fig. 8 along with μ^{115}Sn = −10 (i.e. the average of all the measured terrestrial basalts). Since the highest estimates for In/Sn_{BSE} do not fit on the trend defined by the chondritic samples, our data favor a relative low In/Sn_{BSE} of about 0.10, which is however, significantly higher than the In/Sn of chondrites. This represents independent evidence for a suprachondritic In/Sn_{BSE}. A suprachondritic In/Sn_{BSE} is in contrast to what is predicted by a monotonous depletion of volatile elements with decreasing half-condensation temperature, but it is consistent with previous estimates of the In and Sn contents of the BSE and chondrites (Yi et al., 1995; Witt-Eickschen et al., 2009; Wang et al., 2016). The so called "In overabundance" issue has been matter of debate (e.g., Yi et al., 1995; Witt-Eickschen et al., 2009; Wang et al., 2016; Norris and Wood, 2017). Having independently estimated the In/Sn_{BSE} from μ^{115}Sn data, it is possible to exclude that the relatively high In content is due to sampling or analytical bias. Recently, Braukmüller et al. (2019) suggested a different moderately volatile element depletion trend for Earth, introducing a threshold at a half-mass condensation temperature of 800 K, below which the relative elemental abundance do not show a gradual decline but remains "flat" in chondritic proportion. Such a hockey stick-like pattern was first observed in chondrites (Takahashi et al., 1978; Braukmüller et al., 2018) and later considered for Earth (Braukmüller et al., 2019). According to this model, the In mass fraction of the BSE is inherited from chondritic building blocks. The lower relative BSE abundance of similarly volatile elements is due to their variable partitioning into the Earth's core. Thus, lithophile MVE such as Zn and In remained in the silicate portion of the Earth, while more siderophile and chalcophile elements (e.g., Cd and Tl) partitioned partially into the core (Braukmüller et al., 2019). By assuming an In/Sn_{BSE} of 0.10 and that no In partitioned into the core, it is possible to calculate that about 50% of Sn segregated into the core. Experiments have shown that, at the conditions of core formation, Sn is expected to strongly partition into the metal phase, leaving behind a silicate portion extremely depleted in Sn (Ballhaus et al., 2017). Therefore, if only about 50% of Sn is currently contained in the core, most of Sn must have been added to the BSE during the last phases of accretion (e.g., late veneer), when the core was not anymore in equilibrium with the silicate portion of the Earth (Ballhaus et al., 2017).

5. Conclusions

We have developed and tested a new chemical separation protocol for the determination of Sn isotope compositions. Results on terrestrial rocks and chondrites reveal different stable isotope fractionation processes. After instrumental mass bias correction, it was possible to distinguish two types of mass-independent isotope fractionation (MIF) processes. Our data show that both the magnetic isotope and nuclear volume effects play a role and should be considered in Sn isotope studies. Since the effect of MIF processes is mostly observed when comparing odd with even isotopes, particular caution should be taken when mass-dependent isotope fractionation (MDF) processes are inferred using a combination of odd and even isotopes, at least for Sn isotopes. This is particularly important for high-precision studies focused on Sn stable isotope fractionation using a double spike technique as often a mix of odd and even isotopes is used in the spike mixture.

It is not possible to fully exclude that the observed MIF effects were induced during sample preparation and purification and clearly more high precision data for chondrites and terrestrial rocks and further analytical improvements are required. However, the fact that different chondrite groups show unique and distinct isotope fractionation patterns argues against a laboratory-induced isotope fractionation and points towards a geo/cosmochemical origin. The occurrence of MIF in meteorites was previously proposed (Fujii et al., 2006) but it is generally accepted that isotope variations are dominated by nucleosynthetic anomalies, making it difficult to discern the signature of MIF (Moynier et al., 2013; Dauphas and Schauble, 2016). Due to the lack of nucleosynthetic anomalies, Sn and other MVE might represent promising elements to investigate unknown processes in the solar system that were able to produce MIF, in the form of magnetic isotope and nuclear volume effects.

Modelled mass-dependent and mass-independent isotope fractionation processes can successfully reproduce the measured Sn isotope patterns. Friebel et al. (2017) proposed nucleosynthetic variations to explain the pattern of the CM2 Murchison. However, we found that the Murchison data are better reproduced by a nuclear volume effect. Our interpretation is also supported by the isotope patterns of other chondrites, characterized by MIF and no nucleosynthetic variations. The lack of nucleosynthetic variations for Sn isotopes is consistent with observations from other volatile elements such as Se, Cd, Te (Fehr et al., 2006; Labidi et al., 2018; Toth et al., 2020), indicating that s-process variations in the solar system are limited to refractory elements. Likely this is not due to nucleosynthetic processes but to a different history of the carrier phases, because volatile elements did not condense into pre-solar grains after nucleosynthesis in AGB stars (Ek et al., 2020). These observations contrast with nucleosynthetic isotope variations revealed for the lower mass moderately volatile element Zn (Martins et al., 2022; Savage et al., 2022; Steller et al., 2022). The contrasting behaviour may be due to the different stellar sources and/or carrier phases and their history.

We also report the first evidence of ^{115}Sn variations due to the radioactive decay of ^{115}In. The different ^{115}Sn signature of chondrites (and BSE) is consistent with In-Sn fractionation on ordinary chondrite parent bodies in the early solar system. This emphasizes the potential of the ^{115}In-^{115}Sn decay system in tracing planetary processes as well as MVE fractionation in the early solar system. The offset of 150–200 μ^{115}Sn between terrestrial samples and chondrites is consistent with estimates of the In/Sn content of the BSE and confirms the overabundance of In in the BSE when compared to other moderately volatile elements (e.g., Wang et al., 2016). The effect may be explained by carbonaceous chondrite-like MVE depletion pattern of the Earth and partitioning of about 50% of Sn in the Earth core (Braukmüller et al., 2019).

Declaration of Competing Interest

The authors declare that they have no known competing financial interests or personal relationships that could have appeared to influence the work reported in this paper.

Acknowledgements

We thank the associate editor Zaicong Wang for editorial handling and Zhengbin Deng and two anonymous reviewers for providing comments and criticism that helped significantly to improve the manuscript. We thank Steffen Happel (Triskem) for providing information and material about the TBP resin. We also thank John Molloy (NIST) for information on SRM 3161a and SRM 371. We thank Addi Bischoff (University of Münster), Erik Strub (University of Cologne), Glenn McPherson and Tim McCoy (Smithsonian Institute) for providing chondrite samples. This work benefitted from lively and prolific discussions in the geochemistry group of Cologne (J. Tusch, P. Sprung, B. Elfers, E. Hasenstab, M. Pfeiffer, F. Kurzweil, C. Obert, R.O.C Fonseca). We also want to thank Xueying Wang for helpful information during the development of the analytical procedure. This work was supported by the 397 European Commission through ERC grant No. 669666 “Infant Earth” to CM.

Appendix A. Supplementary material

The supplementary material contains: (1) Description of tests performed to check the Sn recovery after evaporation tests in different acid media. The results are shown in Fig. S1. (2) Further considerations on the use of the TBP resin for Sn separation along with different elution curves obtained from different experiments (Fig. S2). (3) Fig. S3 showing the Sn isotope ratio obtained after adding interfering elements; Fig. S4 reporting the Sn isotope pattern of NIST SRM 3161a passed through columns exchange chemistry and added to procedural blanks; Fig. S5 where Sn isotope ratios are reported as function of the estimated procedural yield and amount of processed material. (4) The full dataset with Sn isotope measurements (Table S1) and Sn-In mass fractions (Table S2). Supplementary material to this article can be found online at https://doi.org/10.1016/j.gca.2023.01.014.

References

Akaza, I., Yata, M., 1983. Separation of tin from some metals by extraction chromatography. J. Radioanal. Chem. 78, 255–262.
Akram, W., Schönbächler, M., Bisterzo, S., Gallino, R., 2015. Zirconium isotope evidence for the heterogeneous distribution of s-process materials in the solar system. Geochim. Cosmochim. Acta 165, 484–500.
Alexander, C.M.O., 2019. Quantitative models for the elemental and isotopic fractionations in chondrites: The carbonaceous chondrites. Geochim. Cosmochim. Acta 254, 277–309.
Amari, S., Lewis, R.S., Anders, E., 1995. Interstellar grains in meteorites: III. Graphite and its noble gases. Geochim. Cosmochim. Acta 59, 1411–1426.
Andreasen, R., Sharma, M., 2006. Solar Nebula Heterogeneity in p-Process Samarium and Neodymium Isotopes. Science 314, 806–809.
Andreasen, R., Sharma, M., 2007. Mixing and Homogenization in the Early Solar System: Clues from Sr, Ba, Nd, and Sm Isotopes in Meteorites. ApJ 665, 874–883.
Andris, B., Beňa, J., 2016. The development of 126Sn separation procedure by means of TBP resin. J. Radioanal. Nucl. Chem. 308, 781–788.
Angeli, I., Marinova, K.P., 2013. Table of experimental nuclear ground state charge radii: An update. Atomic Data and Nuclear Data Tables 99, 69–95.
Asai, S., Toshimitsu, M., Hanzawa, Y., Suzuki, H., Shinohara, N., Inagawa, J., Okumura, K., Hotoku, S., Kimura, T., Suzuki, K., Kaneko, S., 2013. Isotope dilution inductively coupled plasma mass spectrometry for determination of 126Sn content in spent nuclear fuel sample. J. Nucl. Sci. Technol. 50, 556–562.
Badullovich, N., Moynier, F., Creech, J., Teng, F.-Z., Sossi, P.A., 2017. Tin isotopic fractionation during igneous differentiation and Earth's mantle composition. Geochem. Perspect. Lett., 24–28
Ballhaus, C., Fonseca, R.O.C., Münker, C., Rohrbach, A., Nagel, T., Speelmanns, I.M., Helmy, H.M., Zirner, A., Vogel, A.K., Heuser, A., 2017. The great sulfur depletion

of Earth's mantle is not a signature of mantle–core equilibration. Contrib. Mineral. Petrol. 172, 68.
Bigeleisen, J., 1996. Nuclear Size and Shape Effects in Chemical Reactions. Isotope Chemistry of the Heavy Elements. J. Am. Chem. Soc. 118, 3676–3680.
Bisterzo, S., Gallino, R., Straniero, O., Cristallo, S., Käppeler, F., 2010. s-Process in low-metallicity stars – I. Theoretical predictions. MNRAS 404, 1529–1544.
Bisterzo, S., Gallino, R., Straniero, O., Cristallo, S., Käppeler, F., 2011. The s-process in low-metallicity stars - II. Interpretation of high-resolution spectroscopic observations with asymptotic giant branch models. MNRAS 418, 284–319.
Bisterzo, S., Travaglio, C., Gallino, R., Wiescher, M., Käppeler, F., 2014. Galactic Chemical Evolution and Solar s-process Abundances: Dependence on the 13C-pocket Structure. ApJ 787, 10.
Braukmüller, N., Wombacher, F., Hezel, D.C., Escoube, R., Münker, C., 2018. The chemical composition of carbonaceous chondrites: Implications for volatile element depletion, complementarity and alteration. Geochim. Cosmochim. Acta 239, 17–48.
Braukmüller, N., Wombacher, F., Funk, C., Münker, C., 2019. Earth's volatile element depletion pattern inherited from a carbonaceous chondrite-like source. Nat. Geosci. 12, 564–568.
Braukmüller, N., Wombacher, F., Bragagni, A., Münker, C., 2020. Determination of Cu, Zn, Ga, Ag, Cd, In, Sn and Tl in Geological Reference Materials and Chondrites by Isotope Dilution ICP-MS. Geostand. Geoanal. Res. 44, 733–752.
Buchachenko, A.L., 2013. Mass-Independent Isotope Effects. J. Phys. Chem. B 117, 2231–2238.
Buchachenko, A.L., 2018. Magnetic isotopes as a means to elucidate Earth and environmental chemistry. Russ. Chem. Rev. 87, 727.
Burkhardt, C., Kleine, T., Oberli, F., Pack, A., Bourdon, B., Wieler, R., 2011. Molybdenum isotope anomalies in meteorites: Constraints on solar nebula evolution and origin of the Earth. Earth Planet. Sci. Lett. 312, 390–400.
Burkhardt, C., Kleine, T., Dauphas, N., Wieler, R., 2012a. Nucleosynthetic Tungsten Isotope Anomalies in Acid Leachates of the Murchison Chondrite: Implications for Hafnium-Tungsten Chronometry. ApJL 753, L6.
Burkhardt, C., Kleine, T., Dauphas, N., Wieler, R., 2012b. Origin of isotopic heterogeneity in the solar nebula by thermal processing and mixing of nebular dust. Earth Planet. Sci. Lett. 357–358, 298–307.
Burkhardt, C., Dauphas, N., Hans, U., Bourdon, B., Kleine, T., 2019. Elemental and isotopic variability in solar system materials by mixing and processing of primordial disk reservoirs. Geochim. Cosmochim. Acta 261, 145–170.
Carlson, R.W., Boyet, M., Horan, M., 2007. Chondrite Barium, Neodymium, and Samarium Isotopic Heterogeneity and Early Earth Differentiation. Science 316, 1175–1178.
Chen, J.H., Papanastassiou, D.A., Wasserburg, G.J., 2010. Ruthenium endemic isotope effects in chondrites and differentiated meteorites. Geochim. Cosmochim. Acta 74, 3851–3862.
Creech, J.B., Moynier, F., 2019. Tin and zinc stable isotope characterisation of chondrites and implications for early Solar System evolution. Chem. Geol. 511, 81–90.
Creech, J.B., Moynier, F., Badullovich, N., 2017. Tin stable isotope analysis of geological materials by double-spike MC-ICPMS. Chem. Geol. 457, 61–67.
Dauphas, N., Marty, B., Reisberg, L., 2002. Molybdenum Evidence for Inherited Planetary Scale Isotope Heterogeneity of the Protosolar Nebula. ApJ 565, 640–644.
Dauphas, N., Davis, A.M., Marty, B., Reisberg, L., 2004. The cosmic molybdenum–ruthenium isotope correlation. Earth Planet. Sci. Lett. 226, 465–475.
Dauphas, N., Burkhardt, C., Warren, P.H., Fang-Zhen, T., 2014. Geochemical arguments for an Earth-like Moon-forming impactor. Phil. Trans. R. Soc. A 372, 20130244.
Dauphas, N., Schauble, E.A., 2016. Mass Fractionation Laws, Mass-Independent Effects, and Isotopic Anomalies. Annu. Rev. Earth Planet. Sci. 44, 709–783.
De Laeter, J.R., Jeffery, P.M., 1965. The isotopic composition of terrestrial and meteoritic tin. J. Geophys. Res. 70, 2895–2903.
Devillers, C., Lecomte, T., Hagemann, R., 1983. Absolute isotope abundances of tin. Int. J. Mass Spectrom. Ion Phys. 50, 205–217.
Dillmann, I., Käppeler, F., Rauscher, T., Thielemann, F.K., Gallino, R., Bisterzo, S., 2008. Are there only 30 p-nuclei. Proc. Sci.
Dirks, C., Vajda, N., Kovács-Széles, E., Bombard, A., Happel, S., 2014. Characteristic of a TBP resin and its application to the separation of Sn. In: Proceedings of 17th Radiochemistry conference Radiochemistry conference. Mariánske Lázně – Czech Republic.
Ek, M., Hunt, A.C., Lugaro, M., Schönbächler, M., 2020. The origin of s -process isotope heterogeneity in the solar protoplanetary disk. Nat. Astron 4, 273–281.
Elfers, B.-M., Sprung, P., Pfeifer, M., Wombacher, F., Peters, S.T.M., Münker, C., 2018. Variable distribution of s-process Hf and W isotope carriers in chondritic meteorites – Evidence from 174Hf and 180W. Geochim. Cosmochim. Acta 239, 346–362.
Elfers, B.-M., Sprung, P., Messling, N., Münker, C., 2020. The combined Zr and Hf isotope inventory of bulk rock and sequentially leached chondrite samples. Geochim. Cosmochim. Acta 270, 475–491.
Epov, N.V., 2011. Magnetic isotope effect and theory of atomic orbital hybridization to predict a mechanism of chemical exchange reactions. Phys. Chem. Chem. Phys. 13, 13222–13231.
Epov, N.V., Malinovskiy, D., Vanhaecke, F., Bégué, D., Donard, F.X.O., 2011. Modern mass spectrometry for studying mass-independent fractionation of heavy stable isotopes in environmental and biological sciences. J. Anal. At. Spectrom 26, 1142–1156.
Esat, T.M., Spear, R.H., Taylor, S.R., 1986. Isotope anomalies induced in laboratory distillation. Nature 319, 576–578.
Fehr, M.A., Rehkämper, M., Halliday, A.N., Schönbächler, M., Hattendorf, B., Günther, D., 2006. Search for nucleosynthetic and radiogenic tellurium isotope anomalies in carbonaceous chondrites. Geochim. Cosmochim. Acta 70, 3436–3448.
Fehr, M.A., Rehkämper, M., Halliday, A.N., Hattendorf, B., Günther, D., 2009. Tellurium isotope compositions of calcium-aluminum-rich inclusions. Meteorit. Planet. Sci. 44, 971–984.
Fischer-Gödde, M., Burkhardt, C., Kruijer, T.S., Kleine, T., 2015. Ru isotope heterogeneity in the solar protoplanetary disk. Geochim. Cosmochim. Acta 168, 151–171.
Friebel, M., Schönbächler, M., Fehr, M.A., Toth, E.R., 2017. Nucleosynthetic tin isotope variations in chondrites. In: Goldschmidt Conference. Paris. p. 1215.
Friebel, M., Toth, E.R., Fehr, M.A., Schönbächler, M., 2020. Efficient separation and high-precision analyses of tin and cadmium isotopes in geological materials. J. Anal. At. Spectrom. 35, 273–292.
Fujii, T., Moynier, F., Albarède, F., 2006. Nuclear field vs. nucleosynthetic effects as cause of isotopic anomalies in the early Solar System. Earth Planet. Sci. Lett. 247, 1–9.
Fukami, Y., Yokoyama, T., 2017. Tellurium isotope compositions in acid leach fractions of carbonaceous chondrites. Geochem. J. 51, 17–29.
Hayakawa, T., Shizuma, T., Chiba, S., Kajino, T., Hatsukawa, Y., Iwamoto, N., Shinohara, N., Harada, H., 2009. Neutron Capture Cross Section to 113Cd Isomer and s-Process Contribution to Rare p-Nuclide 115Sn. ApJ 707, 859.
Hellmann, J.L., Hopp, T., Burkhardt, C., Kleine, T., 2020. Origin of volatile element depletion among carbonaceous chondrites. Earth Planet. Sci. Lett. 549, 116508.
Hidaka, H., Ebihara, M., Yoneda, S., 2000a. Isotopic study of neutron capture effects on Sm and Gd in chondrites. Earth Planet. Sci. Lett. 180, 29–37.
Hidaka, H., Ebihara, M., Yoneda, S., 2000b. Neutron capture effects on samarium, europium, and gadolinium in Apollo 15 deep drill-core samples. Meteorit. Planet. Sci. 35, 581–589.
Hidaka, H., Ohta, Y., Yoneda, S., 2003. Nucleosynthetic components of the early solar system inferred from Ba isotopic compositions in carbonaceous chondrites. Earth Planet. Sci. Lett. 214, 455–466.
Hutchison, M.A., Bodénan, J.-D., Mayer, L., Schönbächler, M., 2022. Presolar grain dynamics: Creating nucleosynthetic variations through a combination of drag and viscous evolution. MNRAS 512, 5874–5894.
Ireland, T.R., Ávila, J.N., Lugaro, M., Cristallo, S., Holden, P., Lanc, P., Nittler, L., Alexander, C.M.O., Gyngard, F., Amari, S., 2018. Rare earth element abundances in presolar SiC. Geochim. Cosmochim. Acta 221, 200–218.
Jochum, K.P., Hofmann, A.W., Seufert, H.M., 1993. Tin in mantle-derived rocks: Constraints on Earth evolution. Geochim. Cosmochim. Acta 57, 3585–3595.
Kirchenbaur, M., Münker, C., Schuth, S., Garbe-Schönberg, D., Marchev, P., 2012. Tectonomagmatic Constraints on the Sources of Eastern Mediterranean K-rich Lavas. J. Petrol. 53, 27–65.
Kirchenbaur, M., Heuser, A., Bragagni, A., Wombacher, F., 2018. Determination of In and Sn Mass Fractions in Sixteen Geological Reference Materials by Isotope Dilution MC-ICP-MS. Geostand. Geoanal. Res. 42, 361–377.
Kurzweil, F., Münker, C., Grupp, M., Braukmüller, N., Fechtner, L., Christian, M., Hohl, S.V., Schoenberg, R., 2019. The stable tungsten isotope composition of modern igneous reservoirs. Geochim. Cosmochim. Acta 251, 176–191.
Labidi, J., König, S., Kurzawa, T., Yierpan, A., Schoenberg, R., 2018. The selenium isotopic variations in chondrites are mass-dependent; Implications for sulfide formation in the early solar system. Earth Planet. Sci. Lett. 481, 212–222.
Lauretta, D.S., Klaue, B., Blum, J.D., Buseck, P.R., 2001. Mercury abundances and isotopic compositions in the Murchison (CM) and Allende (CV) carbonaceous chondrites. Geochim. Cosmochim. Acta 65, 2807–2818.
Lewis, R.S., Ming, T., Wacker, J.F., Anders, E., Steel, E., 1987. Interstellar diamonds in meteorites. Nature 326, 160–162.
Lewis, R.S., Amari, S., Anders, E., 1990. Meteoritic silicon carbide: pristine material from carbon stars. Nature 348, 293–298.
Lewis, R.S., Amari, S., Anders, E., 1994. Interstellar grains in meteorites: II. SiC and its noble gases. Geochim. Cosmochim. Acta 58, 471–494.
Leya, I., Masarik, J., 2013. Thermal neutron capture effects in radioactive and stable nuclide systems. Meteorit. Planet. Sci. 48, 665–685.
Lingenfelter, R.E., Canfield, E.H., Hampel, V.E., 1972. The lunar neutron flux revisited. Earth Planet. Sci. Lett. 16, 355–369.
Lodders, K., 2003. Solar System Abundances and Condensation Temperatures of the Elements. ApJ 591, 1220.
Lodders, K., Fegley Jr., B., 1997. Complementary Trace Element Abundances in Meteoritic SiC Grains and Carbon Star Atmospheres. Astrophys. J. Lett. 484, L71–L74.
Loss, R.D., Rosman, K.J.R., de Laeter, J.R., 1990. The isotopic composition of zinc, palladium, silver, cadmium, tin, and tellurium in acid-etched residues of the Allende meteorite. Geochim. Cosmochim. Acta 54, 3525–3536.
Lugaro, M., Cseh, B., Világos, B., Karakas, A.I., Ventura, P., Dell'Agli, F., Trappitsch, R., Hampel, M., D'Orazi, V., Pereira, C.B., Tagliente, G., Szabó, G.M., Pignatari, M., Battino, U., Tattersall, A., Ek, M., Schönbächler, M., Hron, J., Nittler, L.R., 2020. Origin of Large Meteoritic SiC Stardust Grains in Metal-rich AGB Stars. ApJ 898, 96.
Malinovskiy, D., Moens, L., Vanhaecke, F., 2009. Isotopic fractionation of Sn during methylation and demethylation reactions in aqueous solution. Environ. Sci. Technol. 43, 4399–4404.
Maréchal, C.N., Télouk, P., Albarède, F., 1999. Precise analysis of copper and zinc isotopic compositions by plasma-source mass spectrometry. Chem. Geol. 156, 251–273.

Martins, R., Kuthning, S., Coles, B.J., Kreissig, K., Rehkämper, M., 2022. Nucleosynthetic Zn anomalies reveal the origin of Earth's volatiles. In: 85th Annual Meeting of The Meteoritical Society 2022. p. 6143.
Matsuhisa, Y., Goldsmith, J.R., Clayton, R.N., 1978. Mechanisms of hydrothermal crystallization of quartz at 250°C and 15 kbar. Geochim. Cosmochim. Acta 42, 173–182.
Moynier, F., Fujii, T., Albarède, F., 2009a. Nuclear field shift effect as a possible cause of Te isotopic anomalies in the early solar system—An alternative explanation of Fehr et al. (2006 and 2009). Meteorit. Planet. Sci. 44, 1735–1742.
Moynier, F., Fujii, T., Telouk, P., 2009b. Mass-independent isotopic fractionation of tin in chemical exchange reaction using a crown ether. Anal. Chim. Acta 632, 234–239.
Moynier, F., Fujii, T., Brennecka, G.A., Nielsen, S.G., 2013. Nuclear field shift in natural environments. C. R. Geosci. 345, 150–159.
Mughabghab, S.F. (Ed.), 2018. Recommended Thermal Cross Sections, Resonance Properties, and Resonance Parameters for Z = 1–60. In: Atlas of Neutron Resonances (Sixth Edition) Elsevier, Amsterdam. pp. 89–822.
Netterdon, L., Mayer, J., Scholz, P., Zilges, A., 2015. Total and partial cross sections of the 112Sn(α, γ)116Te reaction measured via in-beam γ -ray spectroscopy. Phys. Rev. C 91, 035801.
Nielsen, S.G., Auro, M., Righter, K., Davis, D., Prytulak, J., Wu, F., Owens, J.D., 2019. Nucleosynthetic vanadium isotope heterogeneity of the early solar system recorded in chondritic meteorites. Earth Planet. Sci. Lett. 505, 131–140.
Norris, C.A., Wood, B.J., 2017. Earth's volatile contents established by melting and vaporization. Nature 549, 507–510.
Ott, U., 1993. Interstellar grains in meteorites. Nature 364, 25–33.
Ott, U., 2014. Planetary and pre-solar noble gases in meteorites. Geochemistry 74, 519–544.
Özkan, N., Efe, G., Güray, R.T., Palumbo, A., Görres, J., Lee, H.Y., Lamm, L.O., Rapp, W., Stech, E., Wiescher, M., Gy, G., Zs, F., Somorjai, E., 2007. Astrophysical S factor for alpha-capture on 112Sn in the p-process energy range. Phys. Rev. C 75, 025801.
Palme, H., Lodders, K., Jones, A., 2014. 2.2 - Solar System Abundances of the Elements. In: Treatise on Geochemistry (Second Edition) (ed. H. D. H. K. Turekian). Elsevier, Oxford. pp. 15–36.
Pfeiffer, L., Mills, A.P., Chandross, E.A., Kovacs, T., 1979. Beta spectrum of 115In. Phys. Rev. C 19, 1035–1041.
Pietruszka, A.J., Reznik, A.D., 2008. Identification of a matrix effect in the MC-ICP-MS due to sample purification using ion exchange resin: An isotopic case study of molybdenum. Int. J. Mass Spectrom. 270, 23–30.
Polyakov, V.B., Mineev, S.D., Clayton, R.N., Hu, G., Mineev, K.S., 2005. Determination of tin equilibrium isotope fractionation factors from synchrotron radiation experiments. Geochim. Cosmochim. Acta 69, 5531–5536.
Qin, L., Alexander, C.M.O., Carlson, R.W., Horan, M.F., Yokoyama, T., 2010. Contributors to chromium isotope variation of meteorites. Geochim. Cosmochim. Acta 74, 1122–1145.
Qin, L., Carlson, R.W., 2016. Nucleosynthetic isotope anomalies and their cosmochemical significance. Geochem. J. 50, 43–65.
Qin, L., Carlson, R.W., Alexander, C.M.O., 2011. Correlated nucleosynthetic isotopic variability in Cr, Sr, Ba, Sm, Nd and Hf in Murchison and QUE 97008. Geochim. Cosmochim. Acta 75, 7806–7828.
Regelous, M., Elliott, T., Coath, C.D., 2008. Nickel isotope heterogeneity in the early Solar System. Earth Planet. Sci. Lett. 272, 330–338.
Reisberg, L., Dauphas, N., Luguet, A., Pearson, D.G., Gallino, R., Zimmermann, C., 2009. Nucleosynthetic osmium isotope anomalies in acid leachates of the Murchison meteorite. Earth Planet. Sci. Lett. 277, 334–344.
Reynolds, J.H., Turner, G., 1964. Rare gases in the chondrite Renazzo. J. Geophys. Res. 1896–1977 (69), 3263–3281.
Rotaru, M., Birck, J.L., Allègre, C.J., 1992. Clues to early Solar System history from chromium isotopes in carbonaceous chondrites. Nature 358, 465–470.
Russell, W.A., Papanastassiou, D.A., Tombrello, T.A., 1978. Ca isotope fractionation on the Earth and other solar system materials. Geochim. Cosmochim. Acta 42, 1075–1090.
Savage, P.S., Moynier, F., Boyet, M., 2022. Zinc isotope anomalies in primitive meteorites identify the outer solar system as an important source of Earth's volatile inventory. Icarus 386, 115172.
Schauble, E.A., 2004. Applying Stable Isotope Fractionation Theory to New Systems. Rev. Mineral. Geochem. 55, 65–111.
Schauble, E.A., 2007. Role of nuclear volume in driving equilibrium stable isotope fractionation of mercury, thallium, and other very heavy elements. Geochim. Cosmochim. Acta 71, 2170–2189.
Schauble, E.A., 2013. Modeling nuclear volume isotope effects in crystals. PNAS 110, 17714–17719.
Schiller, M., Paton, C., Bizzarro, M., 2015. Evidence for nucleosynthetic enrichment of the protosolar molecular cloud core by multiple supernova events. Geochim. Cosmochim. Acta 149, 88–102.
Schönbächler, M., Rehkämper, M., Fehr, M.A., Halliday, A.N., Hattendorf, B., Günther, D., 2005. Nucleosynthetic zirconium isotope anomalies in acid leachates of carbonaceous chondrites. Geochim. Cosmochim. Acta 69, 5113–5122.
Shirai, N., Humayun, M., 2011. Mass independent bias in W isotopes in MC-ICP-MS instruments. J. Anal. At. Spectrom. 26, 1414–1420.
Sprung, P., Kleine, T., Scherer, E.E., 2013. Isotopic evidence for chondritic Lu/Hf and Sm/Nd of the Moon. Earth Planet. Sci. Lett. 380, 77–87.
Srinivasan, B., Anders, E., 1978. Noble Gases in the Murchison Meteorite: Possible Relics of s-Process Nucleosynthesis. Science 201, 51–56.
Steele, R.C.J., Coath, C.D., Regelous, M., Russell, S., Elliott, T., 2012. Neutron-poor nickel isotope anomalies in meteorites. ApJ 758, 59.
Steller, T., Burkhardt, C., Yang, C., Kleine, T., 2022. Nucleosynthetic zinc isotope anomalies reveal a dual origin of terrestrial volatiles. Icarus 386, 115171.
Takahashi, H., Janssens, M.-J., Morgan, J.W., Anders, E., 1978. Further studies of trace elements in C3 chondrites. Geochim. Cosmochim. Acta 42, 97–106.
Tielens, A.G.G.M., 2005. The Physics and Chemistry of the Interstellar Medium. Cambridge University Press.
Toth, E.R., Fehr, M.A., Friebel, M., Schönbächler, M., 2020. Cadmium isotopes in chondrites and acid leachates: Nucleosynthetic homogeneity and a monitor for thermal neutron capture effects. Geochim. Cosmochim. Acta 274, 286–301.
Travaglio, C., Hillebrandt, W., Reinecke, M., Thielemann, F.-K., 2004. Nucleosynthesis in multi-dimensional SN Ia explosions. A&A 425, 1029–1040.
Travaglio, C., Röpke, F.K., Gallino, R., Hillebrandt, W., 2011. Type Ia Supernovae as Sites of p-process: Two-Dimensional Models Coupled to Nucleosynthesis. ApJ 739, 93.
Trinquier, A., Birck, J.-L., Allègre, C.J., 2007. Widespread 54Cr Heterogeneity in the Inner Solar System. ApJ 655, 1179.
Trinquier, A., Elliott, T., Ulfbeck, D., Coath, C., Krot, A.N., Bizzarro, M., 2009. Origin of Nucleosynthetic Isotope Heterogeneity in the Solar Protoplanetary Disk. Science 324, 374–376.
Vance, D., Thirlwall, M., 2002. An assessment of mass discrimination in MC-ICPMS using Nd isotopes. Chem. Geol. 185, 227–240.
Verchovsky, A.B., Wright, I.P., Pillinger, C.T., 2003. Ion Implantation into Presolar Grains: A Theoretical Model. Publ. Astron. Soc. Aust. 20, 329–336.
Verchovsky, A.B., Wright, I.P., Pillinger, C.T., 2004. Astrophysical Significance of Asymptotic Giant Branch Stellar Wind Energies Recorded in Meteoritic SiC Grains. ApJ 607, 611.
Wang, X., Fitoussi, C., Bourdon, B., Amet, Q., 2017. A new method of Sn purification and isotopic determination with a double-spike technique for geological and cosmochemical samples. J. Anal. At. Spectrom.
Wang, X., Amet, Q., Fitoussi, C., Bourdon, B., 2018. Tin isotope fractionation during magmatic processes and the isotope composition of the bulk silicate Earth. Geochim. Cosmochim. Acta 228, 320–335.
Wang, X., Fitoussi, C., Bourdon, B., Fegley, B., Charnoz, S., 2019. Tin isotopes indicative of liquid–vapour equilibration and separation in the Moon-forming disk. Nat. Geosci. 12, 707–711.
Wang, X., Fitoussi, C., Bourdon, B., Righter, K., Amet, Q., 2021b. The Sn isotope composition of chondrites: Implications for volatile element depletion in the Solar System. Geochim. Cosmochim. Acta 312, 139–157.
Wang, Z., Laurenz, V., Petitgirard, S., Becker, H., 2016. Earth's moderately volatile element composition may not be chondritic: Evidence from In, Cd and Zn. Earth Planet. Sci. Lett. 435, 136–146.
Wang, T., She, J.-X., Yin, K., Wang, K., Zhang, Y., Lu, X., Liu, X., Li, W., 2021a. Sn(II) chloride speciation and equilibrium Sn isotope fractionation under hydrothermal conditions: A first principles study. Geochim. Cosmochim. Acta 300, 25–43.
Wiederhold, J.G., 2015. Metal Stable Isotope Signatures as Tracers in Environmental Geochemistry. Environ. Sci. Technol. 49, 2606–2624.
Witt-Eickschen, G., Palme, H., O'Neill, H., St, C., Allen, C.M., 2009. The geochemistry of the volatile trace elements As, Cd, Ga, In and Sn in the Earth's mantle: New evidence from in situ analyses of mantle xenoliths. Geochim. Cosmochim. Acta 73, 1755–1778.
Wombacher, F., Rehkämper, M., 2003. Investigation of the mass discrimination of multiple collector ICP-MS using neodymium isotopes and the generalised power law. J. Anal. At. Spectrom. 18, 1371–1375.
Wombacher, F., Rehkämper, M., Mezger, K., 2004. Determination of the mass-dependence of cadmium isotope fractionation during evaporation. Geochim. Cosmochim. Acta 68, 2349–2357.
Wombacher, F., Rehkämper, M., Mezger, K., Bischoff, A., Münker, C., 2008. Cadmium stable isotope cosmochemistry. Geochim. Cosmochim. Acta 72, 646–667.
Wood, B.J., Smythe, D.J., Harrison, T., 2019. The condensation temperatures of the elements: A reappraisal. Am. Mineral. 104, 844–856.
Yamazaki, E., Nakai, S., Yokoyama, T., Ishihara, S., Tang, H., 2013. Tin isotope analysis of cassiterites from Southeastern and Eastern Asia. Geochem. J. 47, 21–35.
Yang, L., Tong, S., Zhou, L., Hu, Z., Mester, Z., Meija, J., 2018. A critical review on isotopic fractionation correction methods for accurate isotope amount ratio measurements by MC-ICP-MS. J. Anal. At. Spectrom 33, 1849–1861.
Yi, W., Halliday, A.N., Lee, D.-C., Christensen, J.N., 1995. Indium and tin in basalts, sulfides, and the mantle. Geochim. Cosmochim. Acta 59, 5081–5090.
Yin, Q.-Z., Lee, C.-T.-A., Ott, U., 2006. Signatures of the s-Process in Presolar Silicon Carbide Grains: Barium through Hafnium. ApJ 647, 676–684.
Young, E.D., Galy, A., Nagahara, H., 2002. Kinetic and equilibrium mass-dependent isotope fractionation laws in nature and their geochemical and cosmochemical significance. Geochim. Cosmochim. Acta 66, 1095–1104.